



# CHORUS

This is the accepted manuscript made available via CHORUS. The article has been published as:

## Order parameters for symmetry-breaking structural transitions: The tetragonal-monoclinic transition in $\text{ZrO}_2$

John C. Thomas and Anton Van der Ven

Phys. Rev. B **96**, 134121 — Published 27 October 2017

DOI: [10.1103/PhysRevB.96.134121](https://doi.org/10.1103/PhysRevB.96.134121)

# Order parameters for symmetry-breaking structural transitions: The tetragonal–monoclinic transition in $\text{ZrO}_2$

John C. Thomas\* and Anton Van der Ven†

*Materials Department, University of California, Santa Barbara, California 93106, USA*

Group/subgroup structural phase transitions are exploited in a wide variety of technologies, including those that rely on shape-memory behavior and on transformation toughening. Here we introduce an approach to identify symmetry-adapted strain and shuffle order parameters for any group/subgroup structural transition between a high symmetry parent phase and its symmetrically equivalent low-symmetry product phases. We show that symmetry-adapted atomic shuffle order parameters can be determined by the diagonalization of an orbital covariance matrix, formed by taking the covariance among the atomic displacement vectors of all symmetrically equivalent product phase variants. We use this approach to analyze the technologically important tetragonal to monoclinic structural phase transformation of  $\text{ZrO}_2$ . We explore the energy landscapes, as calculated with density functional theory, along distinct paths that connect  $m\text{ZrO}_2$  to  $t\text{ZrO}_2$  and to other  $m\text{ZrO}_2$  variants. The calculations indicate favorable pairs of variants and reveal intermediate structures likely to exist at coherent twin boundaries and having relatively low deformation energy. We identify crystallographic features of the monoclinic  $\text{ZrO}_2$  variant that make it very sensitive to shape changing strains.

PACS numbers:

## I. INTRODUCTION

Group/subgroup structural phase transitions occur in a wide variety of crystalline materials. They involve a crystallographic transformation from a high symmetry parent phase, usually stable at high temperature, to a lower symmetry product phase whose space group is a subgroup of that of the parent phase. Group/subgroup structural transitions entail a change of the lattice vectors of the parent crystal and are often also accompanied by an internal shuffle of the atomic positions within the unit cell. Due to the group/subgroup symmetry relation between the parent and product phases, there are always at least two symmetrically equivalent product phases that can form from the same parent crystal<sup>1–4</sup>.

Macroscopic single crystals of the parent phase often decompose into several symmetrically equivalent product phase variants that form a twinned microstructure in order to minimize the otherwise large macroscopic strains that typically accompany a homogeneous transformation. For reversible structural transitions<sup>5</sup>, the twin boundaries of twinned microstructures are usually coherent in the sense that there is crystallographic continuity at the atomic scale when passing from one product phase variant to another variant. This property is beneficial in shape memory applications where the forward and reverse transformations between parent and product phases are repeated over many cycles. It also can allow for facile twin boundary migration in response to external stimuli such as stresses or, if the low symmetry product phase is ferroelectric or magnetic, electric and magnetic fields.

The microstructural evolution during group/subgroup structural transformations can be described at the continuum level with phase field models. A crucial ingredient for such models is a free energy expression that depends on strain as well as relevant order parameters that

describe atomic shuffles. A distinction can be made between two categories of group/subgroup structural transformations. In the first, the primary order parameter is strain. The transformation is driven by a symmetry change of the lattice vectors while the atomic positions within the unit cell only adjust minimally in response to the shape change of the unit cell. The second category of group/subgroup structural transitions is driven by symmetry-breaking internal shuffles of the atoms of the unit cell, accompanied by only minor lattice strains. The first category can be treated with phase field approaches, originally due to Barsch and Krumhansl, in which the free energy surface has multiple local minima corresponding to the low symmetry product phase variants in strain space<sup>6</sup>. The second category can be treated with a generalization of the Allen-Cahn<sup>7</sup> phase-field approach in terms of non-conserved order parameters<sup>8</sup>. In both cases, some set of order parameters is necessary to distinguish the various symmetrically equivalent product phase variants and is defined such that they become zero for the parent phase.

In this paper we introduce an approach to determine symmetry-adapted strain and shuffle order parameters that are specifically tailored for a given martensitic structural transition between a high symmetry parent phase and all of its symmetrically equivalent product phase variants. The approach relies on group-theoretical arguments and only requires knowledge of the structure of the parent and product phases. It yields the minimal set of order parameters that describe both the parent phase and all symmetrically equivalent product phase variants. We apply the approach to analyze the tetragonal-to-monoclinic phase transformation of  $\text{ZrO}_2$ , one of many stable oxides in the Zr–O chemistry<sup>9–13</sup>, and a system whose crystallography is sufficiently complex to demonstrate the utility of the approach.

The  $t\text{ZrO}_2$ - $m\text{ZrO}_2$  phase transformation of  $\text{ZrO}_2$  is a particular martensitic phase transition that is of tremendous importance in a wide variety of applications, including thermal barrier coatings<sup>14-16</sup>, solid electrolytes in oxygen fuel cells<sup>17,18</sup>, and dental restorations<sup>19</sup>. The transformation is exploited to enhance the fracture toughness in  $\text{ZrO}_2$  based ceramics<sup>20-22</sup>. A complex twinned microstructure emerges to self-accommodate the large volume expansion ( $\sim 4\%$ ) and shear that accompany the transformation<sup>23,24</sup>. Although  $m\text{ZrO}_2$  is stable up to  $1170^\circ\text{C}$ , the tetragonal form can remain stable in a thin-film morphology down to temperatures as low as room temperature<sup>25-27</sup>, suggesting that the (meta)stability of  $t\text{ZrO}_2$  may be strongly influenced by strain. In partially stabilized zirconia and tetragonal zirconia polycrystals, nucleation of monoclinic domains, which occurs at lower temperatures, and especially in the presence of moisture<sup>28-30</sup>, is an important mechanism of material degradation. Additionally,  $\text{ZrO}_2$ , crystallographically very similar to  $\text{HfO}_2$ , is a suitable as a high-k dielectric in microelectronic applications<sup>31,32</sup>.

The paper is structured as follows. In Sec. II, we describe the crystallography of the different polymorphs of  $\text{ZrO}_2$  and emphasize the layered nature of  $m\text{ZrO}_2$ , an important crystallographic feature that has so far received little attention. This is followed by the formulation of strain order parameters that conveniently describe the relation between the cubic, tetragonal and monoclinic variants of  $\text{ZrO}_2$ . We then introduce an approach to determine symmetry-adapted shuffle order parameters. In Section III, we explore the energy landscapes, as calculated with density functional theory, along both  $t\text{ZrO}_2 \rightarrow m\text{ZrO}_2$  and  $m\text{ZrO}_2 \rightarrow m\text{ZrO}_2$  pathways. The calculations indicate favorable pairs of variants and reveal intermediate structures that are energetically favorable compared to many other polymorphs of  $\text{ZrO}_2$ .

## II. CRYSTALLOGRAPHY OF GROUP/SUBGROUP STRUCTURAL TRANSITIONS: MONOCLINIC AND $t\text{ZrO}_2$

We describe an approach of constructing symmetry-adapted strain and shuffle order parameters by introducing it within the context of the tetragonal to monoclinic transformation of  $\text{ZrO}_2$ . This transformation serves as a nontrivial example that is both well-known and technologically important. Its crystallography is sufficiently complex as to illustrate the utility of such generalized order parameters for analyzing reversible phase transitions. Therefore, we first describe the crystallographic relationships between the tetragonal and monoclinic polymorphs of  $\text{ZrO}_2$  in some detail before presenting the general approach.

$\text{ZrO}_2$  exists in one of three polymorphs at ambient pressure, depending on its temperature<sup>9</sup>. At high temperatures, it adopts the high symmetry cubic form,  $c\text{ZrO}_2$ , which has a thermally averaged crystal struc-

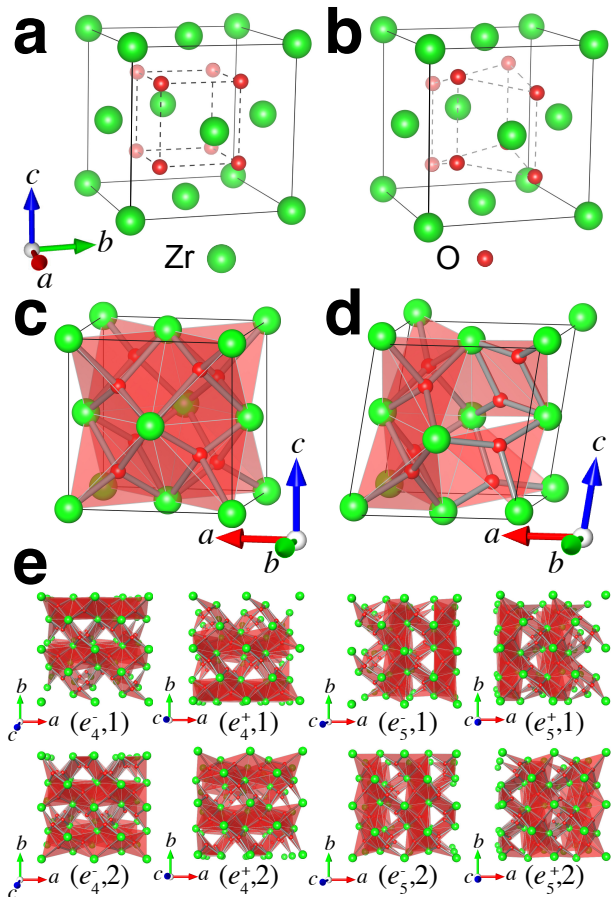


FIG. 1: Ball-and-stick illustrations of the 12-atom conventional cell of (a)  $c\text{ZrO}_2$  and (b)  $t\text{ZrO}_2$ . Polyhedral models of the conventional cell of (c)  $t\text{ZrO}_2$  and (d)  $m\text{ZrO}_2$ , viewed along the  $c$  axis. (e) Polyhedral models of the 8 equivalent variants of the  $m\text{ZrO}_2$  structure depicted in (c), depicted as a  $2 \times 2 \times 2$  supercell of the conventional cell. Polyhedra are centered at tetrahedral O sites.

ture that is identical to  $\text{CaF}_2$  (fluorite). As illustrated in Fig. 1(a),  $c\text{ZrO}_2$  consists of an FCC sublattice of Zr atoms with oxygen filling all of the interstitial tetrahedral sites.  $c\text{ZrO}_2$  undergoes a phase transition upon cooling to a tetragonal form,  $t\text{ZrO}_2$ , shown in Fig. 1(b), whereupon the lattice parameter ratio  $c/a$  becomes greater than one, and the oxygen sublattices undergo a cooperative shuffle, increasing the size of the primitive cell from three atoms in  $c\text{ZrO}_2$  to six in  $t\text{ZrO}_2$ . Half of the (110) planes of oxygen in the conventional unit cell shift along the positive  $c$  direction, with the remaining planes shift along the negative  $c$  direction, thereby forming a checkerboard ordering of up-down shuffled oxygens in the  $a$ - $b$  plane of the tetragonal phase. The conventional cells depicted in Fig. 1(a) and (b) contain 4 and 2 primitive cells, respectively, of  $c\text{ZrO}_2$  and  $t\text{ZrO}_2$ . As the polyhedral model of  $t\text{ZrO}_2$  in Fig. 1 (c) illustrates, the O atoms remain within the tetrahedral interstitial sites in  $t\text{ZrO}_2$ , despite a slight off-centering.

Upon cooling,  $t\text{ZrO}_2$  undergoes an additional transformation to the monoclinic phase,  $m\text{ZrO}_2$ , via a complex cooperative motion involving both the Zr and O sublattices. The transformation is accompanied by a lattice strain that both increases the atomic volume and shears the  $a$ - $c$  plane. The change in periodicity doubles the size of the primitive cell, so that the  $m\text{ZrO}_2$  primitive cell is the 12-atom conventional cell shown in Fig. 1(d). The  $m\text{ZrO}_2$  crystal can be viewed as a layered structure consisting of alternating ‘O4’ sheets, having four-fold coordination of O atoms, and ‘O3’ sheets, having 3-fold coordination of O atoms. The O3 layers are formed as O atoms cooperatively shift away from their tetrahedral sites until they reside within a tetrahedral face. There are a total of eight symmetrically equivalent  $m\text{ZrO}_2$  variants that can form in this way, relative to a particular  $t\text{ZrO}_2$  crystal. Figure 1(e) shows the 8  $m\text{ZrO}_2$  variants that can form from a  $t\text{ZrO}_2$  crystal whose  $c$  axis is parallel to the Cartesian  $z$  axis. Each variant is given a label  $(v, t)$ , where  $v \in \{e_4^+, e_4^-, e_5^+, e_5^-\}$  denotes a shear strain that uniquely specifies the orientation of the crystal relative to  $t\text{ZrO}_2$ , and where  $t \in \{1, 2\}$  distinguishes translational variants (i.e. O3-O4 layering versus O4-O3 layering, relative to the origin).

The displacement of O atoms away from their tetrahedral sites in the O3 layers leaves a fairly open structure when viewed along the  $c$  axis, as can be seen in Fig. 1(e). In  $m\text{ZrO}_2$  each Zr atom is neighbored by 4 O in its adjacent O4 layer but only 3 O in its adjacent O3 layer, for a total coordination of 7. To better accommodate this reduced coordination, the lattice undergoes a monoclinic shear in the  $a$ - $c$  plane, which is compensated by a  $\pm c$  shuffle of  $b$ - $c$  planes of Zr atoms. This combination of shear and Zr displacement allows each O4 layer to locally resemble the  $t\text{ZrO}_2$  structure while the O3 layers concentrate a large portion of the lattice deformation.

In the next two sections, we introduce strain and shuffle order parameters and apply them to describe the crystallographic relationships of the eight symmetrically equivalent  $m\text{ZrO}_2$  variants relative to each other and relative to the  $t\text{ZrO}_2$  parent phase from which they can form.

### A. Strain order parameters and the symmetrically equivalent variants of $m\text{ZrO}_2$

Symmetrically equivalent *orientational* variants of a product phase can be generated by applying the point group operations of the higher-symmetry parent crystal to one replica of the lower-symmetry product crystal. The  $D_{4h}$  point group of  $t\text{ZrO}_2$  contains 16 symmetry elements, while the  $C_{2h}$  point group of  $m\text{ZrO}_2$  is a subgroup of  $D_{4h}$  containing 4 elements. As such, the application of the full tetragonal point group  $D_{4h}$  to the  $m\text{ZrO}_2$  crystal must generate 4 symmetry-equivalent but distinguishable orientations of the  $m\text{ZrO}_2$  phase. Additional *translational* variants emerge if the primitive cell

of the product phase is a supercell of the parent primitive cell. For each of the four orientational variants of  $m\text{ZrO}_2$  there are two additional translational variants. This two-fold multiplicity is due to the periodicity doubling that occurs during the  $t\text{ZrO}_2$ - $m\text{ZrO}_2$  transition.

We define strain order parameters that can distinguish orientational variants of the product phase by measuring deformation of the crystal relative to the parent phase<sup>33</sup>. A particular unit cell of the crystal is specified by the  $3 \times 3$  matrix  $\mathbf{L}$ , whose columns are 3 lattice vectors of the crystal. A finite homogeneous deformation of the crystal deforms the lattice vectors according to  $\mathbf{L}' = \mathbf{U}\mathbf{L}$ , where the right stretch tensor,  $\mathbf{U}$ , is a symmetric, positive-definite  $3 \times 3$  matrix. We define the six-dimensional vector of symmetry-adapted strain order parameters

$$\vec{e} = \begin{pmatrix} e_1 \\ e_2 \\ e_3 \\ e_4 \\ e_5 \\ e_6 \end{pmatrix} \equiv \begin{pmatrix} (H_{xx} + H_{yy} + H_{zz})/\sqrt{3} \\ (H_{xx} - H_{yy})/\sqrt{2} \\ (2H_{zz} - H_{xx} - H_{yy})/\sqrt{6} \\ \sqrt{2}H_{yz} \\ \sqrt{2}H_{xz} \\ \sqrt{2}H_{xy} \end{pmatrix}, \quad (1)$$

where  $H_{i,j}$  is an element of the Hencky strain tensor, which is defined as the matrix logarithm of  $\mathbf{U}$ . Given the eigendecomposition  $\mathbf{U} = \mathbf{V}\mathbf{\Sigma}\mathbf{V}^\top$ , the Hencky strain is thus the symmetric matrix  $\mathbf{H} = \mathbf{V} \ln(\mathbf{\Sigma}) \mathbf{V}^\top$ . The high symmetry parent crystal structure is the reference relative to which strains are measured, such that  $\mathbf{H} = \mathbf{0}$  for the parent crystal. Importantly, the Hencky strain describes volumetric crystal deformations (which are wholly captured by  $e_1$ ) independently from shape changing (and volume preserving) deformations.

The symmetry-adapted strain order parameters,  $\vec{e}$ , are especially convenient for identifying symmetry breaking distortions of the crystal accompanying group/subgroup structural transitions. Considering a cubic crystal with its cubic axes aligned along the Cartesian coordinate axes, the first order parameter,  $e_1$ , describes symmetry preserving volumetric changes of the crystal. The order parameters  $e_2$  and  $e_3$  together describe cubic-tetragonal and cubic-orthorhombic symmetry-breaking in a  $2D$  subspace. This is illustrated in Fig. 2(a), in which the origin corresponds to the cubic reference crystal and the solid (dashed) lines correspond to three symmetrically equivalent compressive (tensile) tetragonal distortions. Any point off the dashed or solid lines corresponds to an orthorhombic distortion of the cubic reference crystal. The last three strain order parameters,  $e_4$ ,  $e_5$ , and  $e_6$ , correspond to shear deformations and together describe orthorhombic, rhombohedral, monoclinic, and triclinic symmetry-breaking of the cubic reference crystal in a  $3D$  subspace<sup>33</sup>.

The strain order parameters allow intuitive depictions of symmetric relationships among different variants of the parent and product phases. Figure 2(a) shows the relationship of the three equivalent tetragonal forms of  $\text{ZrO}_2$  ( $c/a > 1$ , represented by blue diamonds), relative

to the cubic crystal (corresponding to the origin), projected into the  $e_2$ - $e_3$  plane. The  $x$ -,  $y$ -, and  $z$ -oriented  $t\text{ZrO}_2$  variants reside at vertices of an equilateral triangle in the  $e_2$ - $e_3$  plane. The diamond labeled  $z$  in Fig. 2(a) corresponds to a  $t\text{ZrO}_2$  variant having its  $c$  axis aligned along the Cartesian  $z$  axis.

The application of additional symmetry-breaking strains to the  $t\text{ZrO}_2$  variant labeled  $z$  in Fig. 2(a) yields the symmetrically equivalent variants of the product  $m\text{ZrO}_2$  phase. Deforming  $t\text{ZrO}_2$  along  $+e_2$  ( $-e_2$ ) produces a crystal with orthorhombic symmetry by lengthening (shortening) the  $x$ -oriented  $a$  lattice parameter and shortening (lengthening) the  $y$ -oriented  $b$  lattice parameter, yielding the green square  $z_x$  ( $z_y$ ) in Fig. 2(a). The  $z_x$  and  $z_y$  deformations are symmetrically equivalent relative to the  $z$ -oriented  $t\text{ZrO}_2$ . Each orthorhombic strain has 6-fold multiplicity relative to cubic symmetry, as illustrated by the six green squares in Fig. 2(a). Further deforming the orthorhombic crystal at either of the points  $z_x$  or  $z_y$  in Fig. 2(a) along  $\pm e_4$  or  $\pm e_5$ , respectively, yields the monoclinic lattice of a particular  $m\text{ZrO}_2$  variant, which can be uniquely specified in  $(e_2, e_4, e_5)$  space. Figure 2(b) shows the four orientational variants of  $m\text{ZrO}_2$  that can be obtained in this way. These four variants are labeled  $e_4^-, e_4^+, e_5^-,$  and  $e_5^+$ , according to their shear strain order parameter values.

### B. Construction and description of monoclinic order parameters

Although strain order parameters can distinguish orientational variants of the product phase, additional order parameters are needed to distinguish between product phase variants that differ only in their atomic shuffles. These shuffle order parameters are important descriptors of structural transitions that are driven by symmetry-breaking phonon mode instabilities. In this section we develop a general approach to construct a minimal set of shuffle order parameters that can distinguish all symmetrically equivalent shuffle displacement fields and that are zero in the high symmetry parent phase. We first develop the approach in the absence of any strains of the parent crystal structure and focus only on the atomic shuffle displacements. We then describe how this restriction can be relaxed to generate a minimal set of order parameters that also describes symmetry breaking strains of the parent crystal structure.

We start by developing mathematical expressions for the application of symmetry to atomic coordinates of the parent crystal. The atomic coordinates within a particular periodic unit cell of the parent crystal containing  $N$  atoms can be considered as the columns of a  $3 \times N$  matrix  $\mathbf{R} = (\vec{r}_1 | \dots | \vec{r}_N)$ . The application of a space-group operation  $\hat{s}$  of the high symmetry parent crystal is given by the affine transformation  $\mathbf{S}(\hat{s})\mathbf{R} + \vec{\tau}(\hat{s})\vec{1}^{(N)\top}$ , where  $\mathbf{S}(\hat{s})$  is a  $3 \times 3$  symmetry matrix describing a rotation, reflection, inversion, rotoinversion, or identity operation,

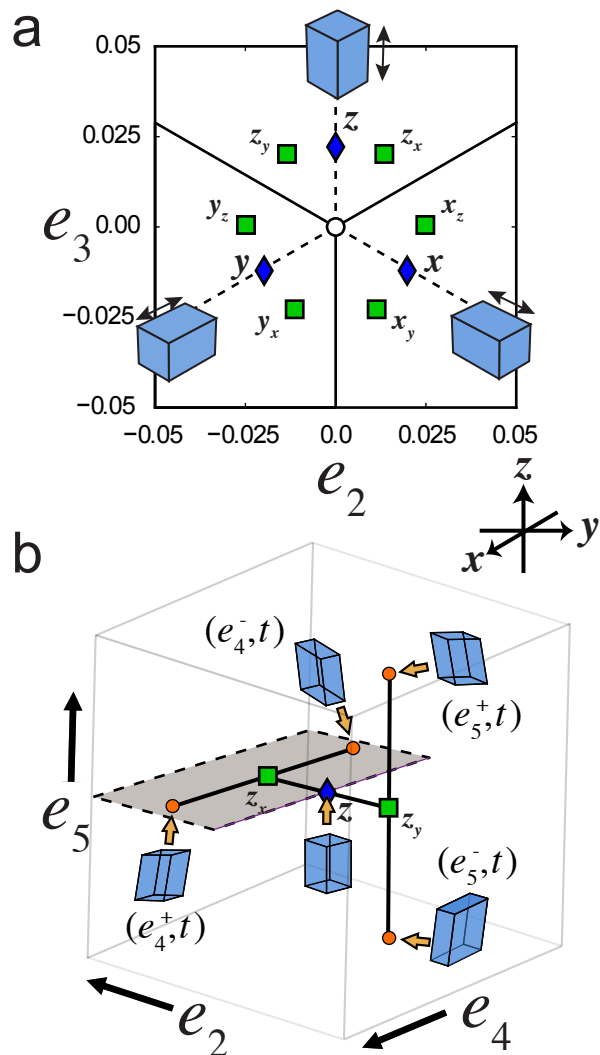


FIG. 2: Illustration of relationships among the conventional cells of cubic, tetragonal, and monoclinic  $\text{ZrO}_2$ . (a) Homogeneous lattice strains, relative to  $c\text{ZrO}_2$ , realized by the cubic, tetragonal, and monoclinic phases, projected into the  $e_2$ - $e_3$  plane of deviatoric strain. Within this plane, the diamond labeled ‘ $z$ ’ corresponds to a tetragonal strain with major axis along  $z$ , and squares labeled  $z_x$  and  $z_y$  are orthorhombic strains of  $z$  with semimajor axis along  $x$  and  $y$ , respectively. (b) Homogeneous lattice strains, relative to  $t\text{ZrO}_2$ , realized by the tetragonal, and monoclinic phases, projected into the  $e_2$ - $e_3$  plane of deviatoric strain. The diamond labeled ‘ $z$ ’ in (a) corresponds to the origin of (b).

$\vec{\tau}(\hat{s})$  is a  $3 \times 1$  translation vector, and  $\vec{1}^{(N)}$  is a  $N \times 1$  vector of ones. Because  $\hat{s}$  is in the space group of the crystal, the transformed coordinates will map back onto the original coordinates of the crystal to within a translation of the unit cell lattice vectors  $\mathbf{L}$ . We introduce the notation  $\hat{s}[\mathbf{R}] = \lfloor \mathbf{S}(\hat{s})\mathbf{R} + \vec{\tau}(\hat{s})\vec{1}^{(N)\top} \rfloor_{\mathbf{L}}$ , where  $\lfloor \cdot \rfloor_{\mathbf{L}}$  specifies a matrix operation wherein a lattice translation is applied to each column of the operand to bring it within the bounds of the unit cell, which need not be the primi-

tive cell of the parent crystal. With this definition, every column of  $\hat{s}[\mathbf{R}]$  must correspond to a column of  $\mathbf{R}$ , although the order of columns may have been permuted. This requires that

$$\hat{s}[\mathbf{R}] = [\mathbf{S}(\hat{s})\mathbf{R} + \vec{\tau}(\hat{s})\vec{\mathbf{1}}^{(N)\top}]_{\mathbf{L}} = \mathbf{R}\mathbf{P}(\hat{s}) \quad (2)$$

where  $\mathbf{P}(\hat{s})$  is a  $N \times N$  permutation matrix of ones and zeros that has exactly one non-zero entry in each column and row. Such permutation matrices are orthogonal, meaning that  $\mathbf{P}(\hat{s})^\top = \mathbf{P}(\hat{s})^{-1}$ . The orthogonality of  $\mathbf{P}(\hat{s})$  leads to the useful invariance relationship

$$\mathbf{R} = [\mathbf{S}(\hat{s})\mathbf{R} + \vec{\tau}(\hat{s})\vec{\mathbf{1}}^{(N)\top}]_{\mathbf{L}}\mathbf{P}(\hat{s})^\top. \quad (3)$$

Having described how symmetry of the parent crystal acts on its ideal coordinates, we shall proceed to consider how symmetry operations act on inhomogeneous displacements of the atomic coordinates. If the ideal positions  $\mathbf{R}$  of the parent crystal are perturbed by a  $(3 \times N)$  displacement matrix, yielding  $\tilde{\mathbf{R}} = \mathbf{R} + \mathbf{D}$ , then direct application of a space-group operation of the parent crystal yields

$$\hat{s}[\tilde{\mathbf{R}}] = [\mathbf{S}(\hat{s})\mathbf{R} + \vec{\tau}(\hat{s})\vec{\mathbf{1}}^{(N)\top}]_{\mathbf{L}} + \mathbf{S}(\hat{s})\mathbf{D}, \quad (4)$$

where, as before, the identities (columns) of the sites have been permuted by  $\mathbf{P}(\hat{s})$ . Using  $\mathbf{P}(\hat{s})$  to return the columns to their original order yields (after substituting the invariance relationship in Eq. (3)),

$$\hat{s}[\tilde{\mathbf{R}}]\mathbf{P}(\hat{s})^\top = \mathbf{R} + \mathbf{S}(\hat{s})\mathbf{D}\mathbf{P}(\hat{s})^\top = \mathbf{R} + \hat{s}[\mathbf{D}], \quad (5)$$

The application of a symmetry operation of the parent crystal to the displacement field  $\mathbf{D}$ , therefore, yields the symmetrically equivalent displacement field  $\hat{s}[\mathbf{D}] = \mathbf{S}(\hat{s})\mathbf{D}\mathbf{P}(\hat{s})^\top$ .

It is convenient to express the displacement field  $\mathbf{D}$  as the  $3N$ -dimensional vector  $\vec{D} = (D_{1,1}, D_{2,1}, \dots, D_{3,N})$ , in which case, application of symmetry to  $\vec{D}$  is given, element-wise, by

$$\hat{s}[\vec{D}]_{(i,j)} = \mathbf{S}(\hat{s})_{i,k} D_{(k,l)} \mathbf{P}(\hat{s})_{j,l} = \mathbf{M}^{(D)}(\hat{s})_{(i,j),(k,l)} D_{(k,l)}. \quad (6)$$

Parentheses are used to denote composite indexing due to the conversion from  $\mathbf{D}$  to  $\vec{D}$ , and the matrix  $\mathbf{M}^{(D)}(\hat{s})_{(i,j),(k,l)} = \mathbf{S}(\hat{s})_{i,k} \mathbf{P}(\hat{s})_{j,l}$ , which is identical to the Kronecker product of  $\mathbf{P}(\hat{s})$  and  $\mathbf{S}(\hat{s})$ , fully describes the effect of  $\hat{s}$  on the displacement field vector  $\vec{D}$ .

We can now proceed to develop an approach that identifies a minimal set of shuffle order parameters relating a high symmetry parent crystal to its symmetrically equivalent product displacement fields. To this end, we equate  $\vec{D}^*$  to the displacement field needed to take the atomic positions of the high symmetry parent phase to one particular variant of the low-symmetry product phase. We can generate the *orbit* of all displacement fields that are

equivalent to a particular  $\vec{D}^*$  by multiplying this displacement field by the matrices  $\mathbf{M}^{(D)}(\hat{s})$  for each space group operation  $\hat{s}$  of the parent crystal, that is unique up to a lattice translation of the unit cell  $\mathbf{L}$ . Because the number of space group operations  $\hat{s}$  in the parent unit cell are finite, there will also only be a finite number  $m$  of symmetrically equivalent displacement fields within the orbit of  $\vec{D}^*$ .

Phase field treatments of reversible structural phase transformations commonly introduce a multidimensional long-range order parameter  $\vec{\xi}$ , with each element  $\xi_i$  corresponding to a particular equivalent variant of the low-symmetry derived phase<sup>34,35</sup>. When the element  $\xi_i = 1$  and all other  $\xi_j = 0$  for  $j \neq i$ ,  $\vec{\xi}$  indicates that the crystal exactly corresponds to the low-symmetry variant  $i$ . The crystal corresponds to the high-symmetry phase when all  $\xi_i = 0$ . The displacement vector for an arbitrary vector  $\vec{\xi}$  is thus  $\vec{d}(\vec{\xi}) = \mathbf{Q}^{(\vec{D}^*)}\vec{\xi}$ , where  $\mathbf{Q}^{(\vec{D}^*)}$  is a  $3N \times m$  matrix whose columns are the members of the orbit of  $\vec{D}^*$ . Taking the scalar product of  $\vec{d}(\vec{\xi})$  with itself yields  $\vec{d}(\vec{\xi})^\top \vec{d}(\vec{\xi}) = \vec{\xi}^\top \mathbf{Q}^{(\vec{D}^*)\top} \mathbf{Q}^{(\vec{D}^*)} \vec{\xi}$ , which, as is shown in Appendix A, is invariant to the symmetry of the parent crystal. This invariance suggests the importance of the  $m \times m$  orbital covariance matrix

$$\mathbf{C}^{(\vec{D}^*)} = \mathbf{Q}^{(\vec{D}^*)\top} \mathbf{Q}^{(\vec{D}^*)}. \quad (7)$$

The orbital covariance matrix is positive semidefinite and symmetric, and, in general, its rank,  $r$ , may be less than  $m$ . As such, we can write it as  $\mathbf{C}^{(\vec{D}^*)} = \mathbf{V}\mathbf{\Lambda}\mathbf{V}^\top$  where  $\mathbf{\Lambda}$  is a  $r \times r$  diagonal matrix of positive real eigenvalues and where  $\mathbf{V}$  is a  $m \times r$  orthogonal matrix whose columns are their corresponding eigenvectors. In this way, we have ignored any eigenvectors of  $\mathbf{C}^{(\vec{D}^*)}$  that have zero eigenvalues. If we define  $\mathbf{B} = \mathbf{\Lambda}^{1/2}\mathbf{V}^\top$  the orbital covariance matrix can then be written as

$$\mathbf{C}^{(\vec{D}^*)} = \mathbf{Q}^{(\vec{D}^*)\top} \mathbf{Q}^{(\vec{D}^*)} = \mathbf{B}^\top \mathbf{B}. \quad (8)$$

This expression motivates the definition of a new  $r$ -dimensional order parameter vector  $\vec{\eta}$ , related to  $\vec{\xi}$  via

$$\vec{\xi} = \mathbf{B}^{-1}\vec{\eta}, \quad \text{and} \quad \vec{\eta} = \mathbf{B}\vec{\xi}, \quad (9)$$

where  $\mathbf{B}^{-1} = \mathbf{V}\mathbf{\Lambda}^{-1/2}$ , such that the inner product expression becomes

$$\vec{d}(\vec{\xi})^\top \vec{d}(\vec{\xi}) = \vec{\xi}^\top \mathbf{B}^\top \mathbf{B} \vec{\xi} = \vec{\eta}^\top \vec{\eta}. \quad (10)$$

The related expression  $\mathbf{Q}^{(\vec{\eta})} = \mathbf{Q}^{(\vec{D}^*)}\mathbf{B}^{-1}$  defines the  $3N \times r$  matrix whose columns are coordinate vectors that describe special symmetry-adapted coordinates in which to express displacements of atoms in the crystal. The order parameter vector  $\vec{\eta} = \mathbf{Q}^{(\vec{\eta})\top} \vec{D}^*$  is thus a  $r$ -dimensional vector whose components are the amplitudes of these coordinates that reproduce  $\vec{D}^*$ . By construction, any element of the orbit of  $\vec{D}^*$  can be written exactly as a

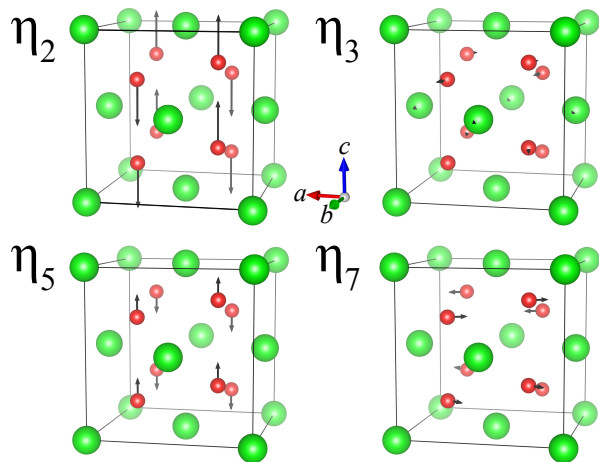


FIG. 3: Depiction of displacement fields due to order parameters  $\eta_2$ ,  $\eta_3$ ,  $\eta_5$ , and  $\eta_7$ . Displacement magnitudes are exaggerated by a factor of 2 to aid visualization.

linear combination of the symmetry-adapted coordinates  $\vec{\eta}$ , but this is not true of an arbitrary displacement field.

The method of identifying internal shuffle order parameters introduced above can easily be extended to generate order parameters that describe both a displacement field  $\vec{D}^*$  and a homogeneous strain  $\vec{e}^*$ . In this more complex scenario, we utilize the compound strain/shuffle vector  $\vec{S}^* = (e_1^*, \dots, e_6^*, D_1^*, \dots, D_{3N}^*)$ , obtained by concatenating the homogeneous strain vector  $\vec{e}^*$  and displacement field vector  $\vec{D}^*$ . The columns of the matrix  $\mathbf{Q}^{(\vec{S}^*)}$  are comprised of these compound vectors for each symmetrically equivalent variant. The symmetry matrices  $\mathbf{M}^{(D)}(\hat{s})$  must be altered slightly to reflect the change in  $\mathbf{Q}^{(\vec{S}^*)}$ .

### C. Qualitative nature of order parameters for the $t\text{ZrO}_2 \rightarrow m\text{ZrO}_2$ transformation

We illustrate the above approach to identifying symmetry-adapted order parameters for the  $t\text{ZrO}_2$  to  $m\text{ZrO}_2$  group/subgroup transformation. The approach generates eight order parameters that can distinguish between  $t\text{ZrO}_2$  and any of the eight variants of  $m\text{ZrO}_2$ . Table I shows the values of the eight order parameters for each  $m\text{ZrO}_2$  variant. Rows of the table correspond to the 8 order parameters and columns correspond to the distinct  $m\text{ZrO}_2$  variants generated by the space group of  $t\text{ZrO}_2$ . Figure 3 shows the displacement fields corresponding to  $\eta_2$ ,  $\eta_3$ ,  $\eta_5$ , and  $\eta_7$ , which, when summed together, yield the  $m\text{ZrO}_2$  internal shuffle for the  $(e_5^-, 1)$  variant.

Each symmetry-adapted order parameter  $\eta_i$  corresponds to the amplitude of a symmetry-adapted displacement field combined with a homogeneous strain. We have normalized the eight order parameter such that they are either  $\pm 1$  or 0 for each monoclinic variant. Table I lists

the RMS strain and RMS atomic displacement contribution for each order parameter in order to quantify the degree to which each order parameter describes either homogeneous or local deformations of the crystal. Order parameters that have a homogeneous strain component or that have the same value for all translational variants of a particular orientational variant correspond to  $\Gamma$ -point collective modes of the crystal, with the associated displacement vector (if it is nonzero) describing an optical-mode polarization vector. Order parameters that do depend on the translation of the product-phase variant (and, thus, cannot have a homogeneous strain component) correspond to non- $\Gamma$  modes in the  $t\text{ZrO}_2$  Brillouin zone. The periodicity-doubling that occurs from  $t\text{ZrO}_2$  to  $m\text{ZrO}_2$  dictates that any non- $\Gamma$  mode must be at the  $M$  point of the  $t\text{ZrO}_2$  Brillouin zone. Based on Table I, we can thus identify  $\eta_1$ - $\eta_4$  as  $\Gamma$ -point modes and  $\eta_5$ - $\eta_8$  as  $M$ -point modes.

Table I also reveals information about the symmetry-breaking properties of each order parameter. For example,  $\eta_2$  has the same value across all variants, and thus must preserve the tetragonal symmetry of the crystal. In contrast,  $\eta_1$  distinguishes between  $e_4$ -type and  $e_5$ -type variants, and thus corresponds exactly to the homogeneous strain order parameter  $e_2$ . Similar arguments allow us to identify  $(\eta_3, \eta_4)$  as describing tetragonal-monoclinic symmetry-breaking at  $\Gamma$ ,  $(\eta_5, \eta_6)$  as describing tetragonal-orthorhombic symmetry-breaking at  $M$ , and  $(\eta_7, \eta_8)$  as describing tetragonal-monoclinic symmetry-breaking at  $M$ .

Although in the example considered here, the dimensionality of the symmetry-adapted order parameter vector,  $\vec{\eta}$ , is exactly equal to the number of  $m\text{ZrO}_2$  variants relative to  $t\text{ZrO}_2$  (i.e. eight), in general there can be more product phase variants than independent order parameters. For example, if we use the higher symmetry  $c\text{ZrO}_2$  crystal as the parent phase instead of  $t\text{ZrO}_2$ , we can describe 6 equivalent  $t\text{ZrO}_2$  variants (comprised of two translational variants for each of the three orientational variants depicted in Fig. 2(a)) and 48 equivalent  $m\text{ZrO}_2$  variants (i.e., 8 for each  $t\text{ZrO}_2$  variant). These variants can all be described within the 12-atom conventional cell, which has 6 strain and 33 displacement degrees of freedom. The space of symmetry-adapted order parameters, therefore, cannot exceed 39 dimensions. In fact, the approach described in the previous section shows that the combined set of 54  $t\text{ZrO}_2$  and  $m\text{ZrO}_2$  variants can all be described within a 30-dimensional order parameter space. In many cases essential thermodynamic features of the structural transition can be captured in a lower-dimensional order parameter space in which all variants are distinguishable, even if some structural information is discarded. In the case of the eight  $m\text{ZrO}_2$  variants relative to  $t\text{ZrO}_2$ , this is possible using as few as four of the symmetry-adapted order parameters shown in Table I (e.g.,  $\eta_3, \eta_4, \eta_5$ , and  $\eta_6$ ).

	$(e_4^-, 1)$	$(e_4^-, 2)$	$(e_4^+, 1)$	$(e_4^+, 2)$	$(e_5^-, 1)$	$(e_5^-, 2)$	$(e_5^+, 1)$	$(e_5^+, 2)$	RMSS	RMSD
$\eta_1$	1	1	1	1	-1	-1	-1	-1	0.011	0.000
$\eta_2$	1	1	1	1	1	1	1	1	0.028	0.143
$\eta_3$	-1	-1	1	1	0	0	0	0	0.121	0.227
$\eta_4$	0	0	0	0	-1	-1	1	1	0.121	0.227
$\eta_5$	1	-1	1	-1	0	0	0	0	0.000	0.290
$\eta_6$	0	0	0	0	1	-1	1	-1	0.000	0.290
$\eta_7$	1	-1	-1	1	0	0	0	0	0.000	0.313
$\eta_8$	0	0	0	0	1	-1	-1	1	0.000	0.313

TABLE I: Table of monoclinic order parameters, evaluated in each of 8  $m\text{ZrO}_2$  variants. Each variant is labeled  $(V, T)$ , where  $V$  labels the monoclinic lattice orientation and  $T$  labels the lattice shift of the monoclinic ordering within the supercell. The RMS strain (RMSS) and RMS atomic displacement (RMSD) of each order parameter coordinate is also shown.

### III. ENERGY LANDSCAPES ALONG PATHS CONNECTING THE PARENT AND SYMMETRICALLY EQUIVALENT PRODUCT VARIANTS

Having established symmetry-adapted strain and shuffle order parameters that can distinguish between  $t\text{ZrO}_2$  and the symmetrically equivalent variants of  $m\text{ZrO}_2$ , we next explore the minimum energy pathways connecting these crystal structures.

Energies were calculated with the PBE parameterization<sup>36</sup> of the generalized gradient approximation to density functional theory as implemented in the Vienna Ab Initio Simulation Package (vasp)<sup>37,38</sup>. Projector augmented wave<sup>38,39</sup> pseudopotentials with valence-electron configurations of  $4s^2, 4p^6, 5s^1, 4d^3$  and  $2s^2, 2p^4$  for Zr and O, respectively, were used. The plane wave basis energy cutoff was set to 600 eV. All calculations were performed in the 12-atom conventional cells of  $\text{ZrO}_2$ , using a  $7 \times 7 \times 7$  Monkhorst-Pack  $k$ -point mesh<sup>40</sup>. Solid-state nudged elastic band (SSNEB) calculations were performed using the vasp Transition State Theory Tools (vtst)<sup>41–43</sup>.

#### A. Energy barriers between symmetrically equivalent monoclinic variants of $\text{ZrO}_2$

The transformation of  $t\text{ZrO}_2$  to  $m\text{ZrO}_2$  often results in a twinned microstructure in which several symmetrically equivalent variants of  $m\text{ZrO}_2$  coexist to self-accommodate the large strains accompanying the structural transformation. The twin boundaries can be coherent, with the crystal structure varying continuously across the boundary. In the vicinity of the boundary, the local atomic environments are no longer monoclinic, resulting in an energy penalty that may be mitigated by local atomic relaxations and a broadening of the boundary. We can obtain a sense of this energy penalty as well as the most favored local crystal structure of coherent twin boundaries by considering the minimum energy paths that connect each symmetrically unique pair of  $m\text{ZrO}_2$  variants.

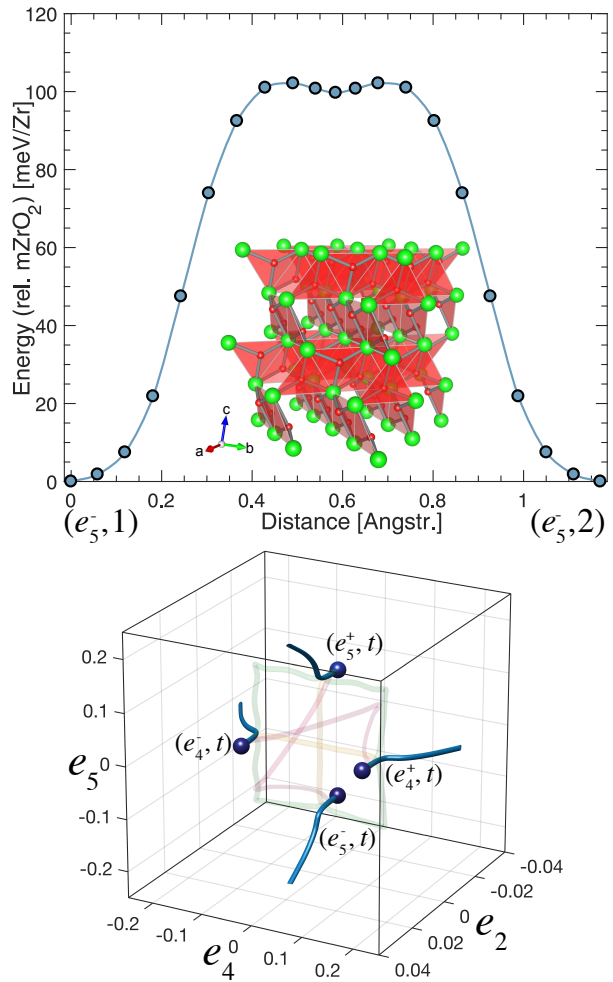


FIG. 4: SSNEB energy barrier between the  $(e_5^-, 1)$  and  $(e_5^-, 2)$   $m\text{ZrO}_2$  variants, illustrated in Fig. 1(e). The structure corresponding to the path midpoint is also depicted.

We calculated the SSNEB minimum energy path for each pair of  $m\text{ZrO}_2$  variants that is distinct relative to the symmetry of the  $z$ -oriented  $t\text{ZrO}_2$  variant. The distinct variant pairs can be represented by the following prototypical examples:  $(e_5^-, 1) \rightarrow (e_5^-, 2)$ , which corresponds

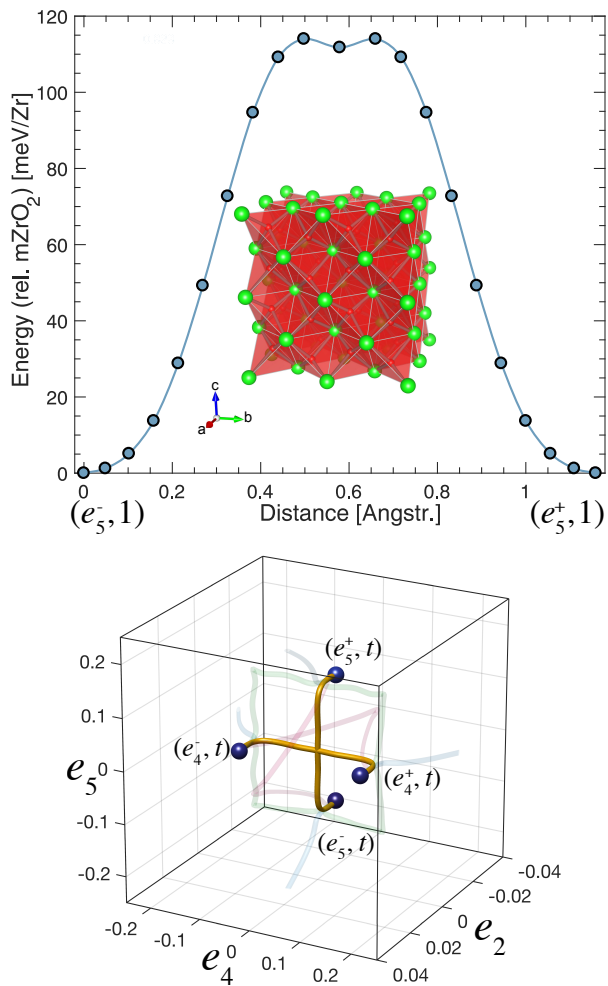


FIG. 5: SSNEB energy barrier between the  $(e_5^-, 1)$  and  $(e_5^+, 1)$   $m\text{ZrO}_2$  variants, illustrated in Fig. 1(e). The structure corresponding to the path midpoint is also depicted.

to a change in translational variant, while fixing orientational variant;  $(e_5^-, 1) \rightarrow (e_5^+, 1)$ , which corresponds to reversing the sign of the monoclinic shear, while fixing the translational variant;  $(e_5^-, 1) \rightarrow (e_5^+, 2)$ , which corresponds to reversing both the translational variant and the sign of the monoclinic shear; and  $(e_5^-, 1) \rightarrow (e_4^-, 1)$ , which corresponds to changing the monoclinic shear plane. Interestingly, the  $(e_5^-, 1) \rightarrow (e_4^-, 1)$  pathway is equivalent to the  $(e_5^-, 1) \rightarrow (e_4^-, 2)$ ,  $(e_5^-, 1) \rightarrow (e_4^+, 1)$ , and  $(e_5^-, 1) \rightarrow (e_4^+, 2)$  pathways, which can be inferred from careful consideration of Figs. 1(e) and 2(b) and inspection of the order parameter values in table I.

Figures 5-7 show the results of SSNEB energy calculations along these prototypical trajectories. Energies are plotted with respect to the generalized per-atom distance along the trajectory, which is calculated between each pair of NEB images using the method described in<sup>43</sup>. This distance metric yields a lower bound on the generalized length of the continuous trajectory. For each trajectory, the relaxed crystal structure of the midpoint

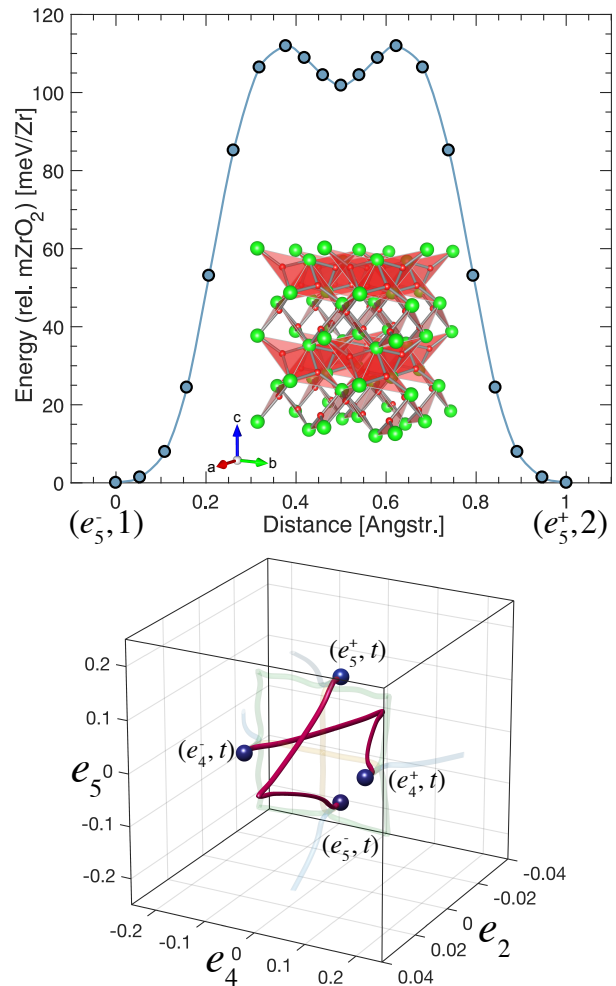


FIG. 6: SSNEB energy barrier between the  $(e_5^-, 1)$  and  $(e_5^+, 2)$   $m\text{ZrO}_2$  variants, illustrated in Fig. 1(e). The structure corresponding to the path midpoint is also depicted.

image is illustrated as an inset. To aid visualization, the orientation of these illustrations is rotated relative to Fig. 1(e). Each trajectory is symmetric about its midpoint, as is clear in Figures 5-7.

Figure 4 shows the SSNEB trajectory from  $(e_5^-, 1)$  to  $(e_5^-, 2)$ , corresponding to reversing the O3–O4 stacking sequence without changing the strain state. If these two variants coexist coherently along the  $[010]_m$  or  $[001]_m$  directions, the transition zone would correspond to an anti-phase boundary, since variants have identical orientations relative to the high symmetry  $t\text{ZrO}_2$  but their internal crystal structures differ by a non-lattice translation along  $[100]_m$ . The energy barrier along  $(e_5^-, 1) \rightarrow (e_5^-, 2)$  is 102 meV/ZrO<sub>2</sub>, while the relaxed midpoint of the  $(e_5^-, 1) \rightarrow (e_5^-, 2)$  trajectory has an energy of 99 meV/ZrO<sub>2</sub> relative to  $m\text{ZrO}_2$ . The structure of the  $(e_5^-, 1) \rightarrow (e_5^-, 2)$  midpoint, shown as an inset in Fig. 4, consists entirely of 3-fold-coordinated oxygen layers that form  $a$ - $b$  planes and alternate between two different orientations along the  $c$  axis. The midpoint has monoclinic point-group symme-

try and is described by a 6-atom primitive cell with an atomic volume 9.7% larger than that of  $m\text{ZrO}_2$ . Furthermore, the  $a$  and  $c$  lattice vectors of the midpoint structure are 5% and 7% longer, respectively, than in the end states. This result suggests that an anti-phase boundary separating  $(e_5^-, 1)$  and  $(e_5^-, 2)$  would locally desire a substantially larger volume than that of the adjacent monoclinic crystals and will be under compressive stresses, thereby having a higher energy than predicted here for the unstressed state.

Figure 4(b) shows the path traveled in  $(e_2, e_4, e_5)$  along the  $(e_5^-, 1) \rightarrow (e_5^-, 2)$  SSNEB trajectory. Since the path connects a pair of  $m\text{ZrO}_2$  variants that differ only by an internal translation, the path starts and ends at the same strain state, corresponding to the  $e_4^-$   $m\text{ZrO}_2$  orientation. Despite this, both the volume-conserving strain order parameters  $e_2$  and  $e_4$  vary substantially along the trajectory from  $(e_5^-, 1)$  to  $(e_5^-, 2)$ . Figure 4(b) also shows all symmetrically equivalent paths.

The SSNEB trajectory from  $(e_5^-, 1)$  to  $(e_5^+, 1)$ , shown in Fig. 5(a), corresponds to reversing the sign of order parameters  $\eta_3$  (which reverses the sign of the monoclinic shear) and  $\eta_7$ . This  $m\text{ZrO}_2$  variant pair can be related as twins across the  $(100)_m$  or  $(001)_m$  plane. The energy barrier along  $(e_5^-, 1) \rightarrow (e_5^+, 1)$  is 114 meV/ $\text{ZrO}_2$ , while the relaxed midpoint structure relaxes to  $t\text{ZrO}_2$  (Fig. 6(a), inset), which has an energy of 112 meV/ $\text{ZrO}_2$  relative to  $m\text{ZrO}_2$ . Figure 6(b) shows the  $(e_2, e_4, e_5)$  pathway corresponding to the  $(e_5^-, 1) \rightarrow (e_5^+, 1)$  SSNEB trajectory. The path passes through the strain state of  $t\text{ZrO}_2$ , the point where the symmetrically equivalent paths intersect. The volume of the intermediate  $t\text{ZrO}_2$  is 6% smaller than that of  $m\text{ZrO}_2$ .

The  $(e_5^-, 1)$  and  $(e_5^+, 2)$   $m\text{ZrO}_2$  variants differ both by a translation of the internal shuffle and the sign of the monoclinic shear strain and can be related as twins across the  $(100)_m$  or  $(001)_m$  plane. Figure 6(a) shows the SSNEB trajectory from  $(e_5^-, 1)$  to  $(e_5^+, 2)$ , corresponding to reversing the sign of order parameters  $\eta_3$  (which reverses the sign of the monoclinic shear) and  $\eta_5$ . The energy barrier along this pathway is 112 meV/ $\text{ZrO}_2$ , while the energy of the relaxed midpoint structure is 102 meV/ $\text{ZrO}_2$  relative to  $m\text{ZrO}_2$ . The structure of the  $(e_5^-, 1) \rightarrow (e_5^+, 2)$  midpoint, shown as an inset in Fig. 5(a), consists entirely of 3-fold-coordinated O and 6-fold-coordinated Zr but exhibits less prominent layering along  $[001]$ , when compared to the  $(e_5^-, 1) \rightarrow (e_5^-, 2)$  midpoint. The midpoint structure has orthorhombic point-group symmetry and is described by a 12-atom primitive cell with an atomic volume 5.6% larger than  $m\text{ZrO}_2$ . The  $(e_2, e_4, e_5)$  pathway corresponding to the  $(e_5^-, 1) \rightarrow (e_5^+, 2)$  SSNEB trajectory, shown in Fig. 5(b) reveals that only  $e_2$  and  $e_4$  are activated, with a significant deviation in the orthorhombic strain order parameter  $e_2$ .

The final symmetrically distinct path describes a change of the active shear order parameter from  $e_4$  to  $e_5$ . Figure 7(a) shows the SSNEB trajectory from  $(e_5^-, 1)$  to  $(e_4^-, 1)$ , corresponding to a deformation that results

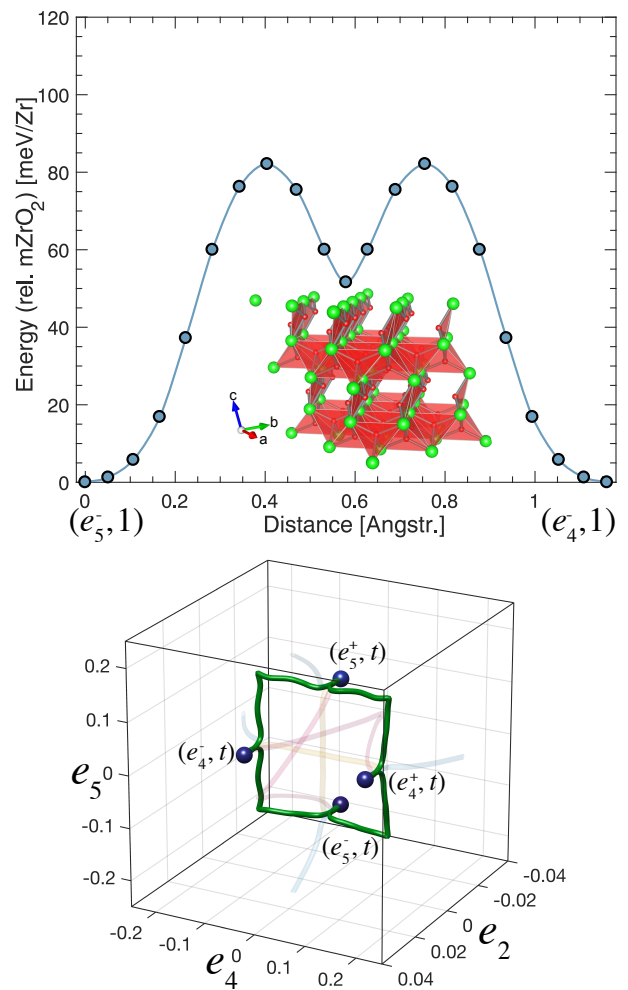


FIG. 7: SSNEB energy barrier between the  $(e_5^-, 1)$  and  $(e_4^-, 1)$   $m\text{ZrO}_2$  variants, illustrated in Fig. 1(e). The structure corresponding to the path midpoint is also depicted. The path is symmetrically equivalent to the paths joining  $(e_5^-, 1)$  to  $(e_5^-, 2)$ ,  $(e_5^+, 1)$ , and  $(e_5^+, 2)$

in an effective  $90^\circ$  rotation of the  $m\text{ZrO}_2$  crystal about the  $c$  axis of the parent  $t\text{ZrO}_2$  crystal. The energy barrier along this pathway is 82 meV/ $\text{ZrO}_2$ , which is significantly lower than the other trajectories between  $m\text{ZrO}_2$  variants. We fully relaxed its structure such that forces were less than  $1 \times 10^{-5}$  eV/ $\text{\AA}$ , and verified its dynamical stability by calculating the  $6 \times 6$  compliance tensor and  $36 \times 36$  ionic Hessian tensor to confirm that neither tensor has negative eigenvalues. The relaxed midpoint of the  $(e_5^-, 1) \rightarrow (e_4^-, 1)$  trajectory, shown as an inset in Fig. 7(a), has an atomic volume within 0.2% of that of  $m\text{ZrO}_2$  and has an energy of 52 meV/ $\text{ZrO}_2$  relative to  $m\text{ZrO}_2$ , which is half that of  $t\text{ZrO}_2$ . The midpoint structure has a 6-atom monoclinic primitive cell, with the monoclinic shear occurring in the  $(1\bar{1}0)$  plane, relative to the crystal axes shown in Fig. 7. It exhibits layering of 3-fold-coordinated and 4-fold-coordinated O atomic layers along its monoclinic  $c$  axis, so that, as in  $m\text{ZrO}_2$ , all Zr atoms

are coordinated by 7 O atoms. This monoclinic structure is very closely related to the orthorhombic polymorph identified in Ref.<sup>44</sup>, which was obtained by relaxing an unstable phonon mode of the volume-expanded  $t\text{ZrO}_2$  crystal. That orthorhombic structure can be constructed by stacking the  $(e_5^-, 1) \rightarrow (e_4^-, 1)$  midpoint structure with its  $(001)_m$  shear-compensating twin, doubling the periodicity of the cell. Figure 7(b) shows the relatively complex path traveled in  $(e_2, e_4, e_5)$  along the  $(e_5^-, 1) \rightarrow (e_4^-, 1)$  trajectory that is necessary to visit the large shear state of the midpoint structure. Due to the symmetry of the  $t\text{ZrO}_2$  parent phase, the  $(e_5^-, 1) \rightarrow (e_4^-, 1)$  pathway is one of 16 equivalent ones from a  $e_4$ -type variant to a  $e_5$ -type variant, regardless of the signs of their monoclinic shear or their relative translations.

### B. The $t\text{ZrO}_2$ - $m\text{ZrO}_2$ transition

Candidate structural pathways for the  $t\text{ZrO}_2 \rightarrow m\text{ZrO}_2$  transition can be identified systematically by considering the symmetrically distinct pairs of  $t\text{ZrO}_2$  and  $m\text{ZrO}_2$  variants. Each distinct structural pathway results in a particular orientation relationship between  $t\text{ZrO}_2$  and  $m\text{ZrO}_2$ . There are three orientation relationships between  $t\text{ZrO}_2$  and  $m\text{ZrO}_2$  that have been extensively discussed in the literature<sup>45</sup>. Each of these can be achieved by a deformation of the tetragonal unit cell followed by a rigid rotation of the resultant monoclinic crystal structure. The first, denoted as Type 1, refers to the  $(001)_m \parallel \{100\}_t$  and  $[010]_m \parallel [001]_t$  orientation relationship, in which the tetragonal lattice vectors  $(\vec{a}^{(t)}, \vec{b}^{(t)}, \vec{c}^{(t)})$  become the monoclinic lattice vectors  $(\vec{c}^{(m)}, \vec{a}^{(m)}, \vec{b}^{(m)})$  after deformation, with  $\vec{b}^{(m)}$  aligned along  $\vec{c}^{(t)}$ <sup>1</sup>. A subsequent small rotation of the  $m\text{ZrO}_2$  crystal by  $\sim 5^\circ$  about  $[010]_m$  then aligns the  $(100)_m$  plane of  $m\text{ZrO}_2$  with the  $(010)_t$  plane of  $t\text{ZrO}_2$ . Type 2 refers to the  $(100)_m \parallel \{100\}_t$  and  $[010]_m \parallel [001]_t$  orientation relationship and can be achieved with an identical deformation of the tetragonal unit cell as that of Type 1, but with a subsequent rotation of  $\sim -5^\circ$  about  $[010]_m$  to align  $(001)_m$  with  $(100)_t$ . Type 3 refers to the  $(100)_m \parallel \{100\}_t$  and  $[010]_m \parallel \langle 010 \rangle_t$  orientation relationship and has the distinction of enabling the closest mapping of the  $m\text{ZrO}_2$  crystal onto the  $t\text{ZrO}_2$  crystal, in a least-squares sense. The relationship between the  $t\text{ZrO}_2$  and  $m\text{ZrO}_2$  crystals as depicted in Fig. 1(c) and 1(d) are an example of the Type 3 orientation relationship.

It is insightful to consider the deformations needed to achieve the different orientation relationships in strain order parameter space. Referring to Fig. 2(a), there are three distinct ways to pair a particular  $t\text{ZrO}_2$  variant (e.g.  $z$ ) with one of the  $m\text{ZrO}_2$  orientational variants that can

emerge from the same  $c\text{ZrO}_2$  crystal (i.e.  $z_x, z_y, x_y, x_z, y_x$  and  $y_z$ ). The  $z \rightarrow z_x$  correspondence is equivalent to the  $z \rightarrow z_y$  correspondence, while the  $z \rightarrow x_z$  and  $z \rightarrow x_y$  are equivalent to the  $z \rightarrow y_z$  and  $z \rightarrow y_x$  correspondences, respectively. The deformation of the tetragonal unit cell to realize the Type 1 and 2 orientation relationships is that of the  $z \rightarrow x_z$  (or equivalently the  $z \rightarrow y_z$ ) correspondence, while the deformation for the Type 3 orientation relationship is that of the  $z \rightarrow z_x$  (or equivalently the  $z \rightarrow z_y$ ) correspondence. The symmetrically distinct  $z \rightarrow x_y$  (or equivalently the  $z \rightarrow y_x$ ) correspondence will result in a distinct  $(100)_m \parallel (001)_t$  and  $[010]_m \parallel [100]_t$  orientation relationship that has not been named in the literature. We will refer to this orientation relationship as ‘Type 4’.

We calculated SSNEB trajectories between each distinct  $t\text{ZrO}_2$ - $m\text{ZrO}_2$  variant pair, relative to  $c\text{ZrO}_2$ , thus capturing all of the different lattice correspondences. Each trajectory was initialized using the linear interpolant from the  $z$   $t\text{ZrO}_2$  variant to a particular variant of  $m\text{ZrO}_2$ . Of these, energies for the trajectories having the lowest barriers are shown in Figs. 8(a)-(c). Figures 8(d)-(g) shows the homogeneous strain along each path, projected into the  $e_2$ - $e_3$  plane of deviatoric strain order parameters.

Although the Type 1/Type 2 orientation relationships are symmetrically distinct from Type 4, all three relationships have degenerate SSNEB pathways, with a 30 meV/Zr barrier relative to  $t\text{ZrO}_2$ . This is shown in Fig. 8(a). By contrast, the SSNEB pathway corresponding to the Type 3 orientation relationship, shown in Fig. 8(b), has an energy barrier of only 2 meV/Zr relative to  $t\text{ZrO}_2$ . This behavior can be understood by considering the SSNEB pathways in strain order parameter space. The Type 1/Type 2 strain pathway (Fig. 8(d)) and the Type 4 strain pathway (Fig. 8(e)) can both be broken into two distinct parts. The first is a pathway between two  $t\text{ZrO}_2$  variants, and the second is a pathway from a  $t\text{ZrO}_2$  variant to one of its nearest  $m\text{ZrO}_2$  variants, which is identical to the Type 3 pathway (Fig. 8(e)). The predicted barriers for the different pathways are consistent with findings in Ref.<sup>46</sup>, and the  $t\text{ZrO}_2$ - $t\text{ZrO}_2$  midpoint structure, whose energy corresponds to the maximum of Fig. 8(a), is nearly identical to the intermediate structure reported in that work. Structural details of the  $t\text{ZrO}_2$ - $t\text{ZrO}_2$  pathway midpoint are reported in the Supplementary Information.

We also considered a trajectory for the Type 3 orientation relationship that passes through the low-energy monoclinic intermediate state in Fig. 7. We denote this trajectory as Type 3b as it is distinct from that of Fig. 8(b) and Fig. 8(e). The Type 3b trajectory, shown in Fig. 8(c), has an energy barrier of less than 1 meV/Zr, relative to  $t\text{ZrO}_2$ , but faces a barrier of 31 meV/Zr to escape the energy well corresponding to the intermediate state. The strain pathway in  $(e_2, e_3)$  space for this trajectory is shown in Fig. 8(g) and deviates only slightly from the Type 3 pathway of Fig. 8(e). This path has sim-

<sup>1</sup> We use the standard convention that  $|\vec{a}^{(m)}| < |\vec{c}^{(m)}|$  and that both  $\vec{a}^{(m)}$  and  $\vec{c}^{(m)}$  are orthogonal to  $\vec{b}^{(m)}$ .

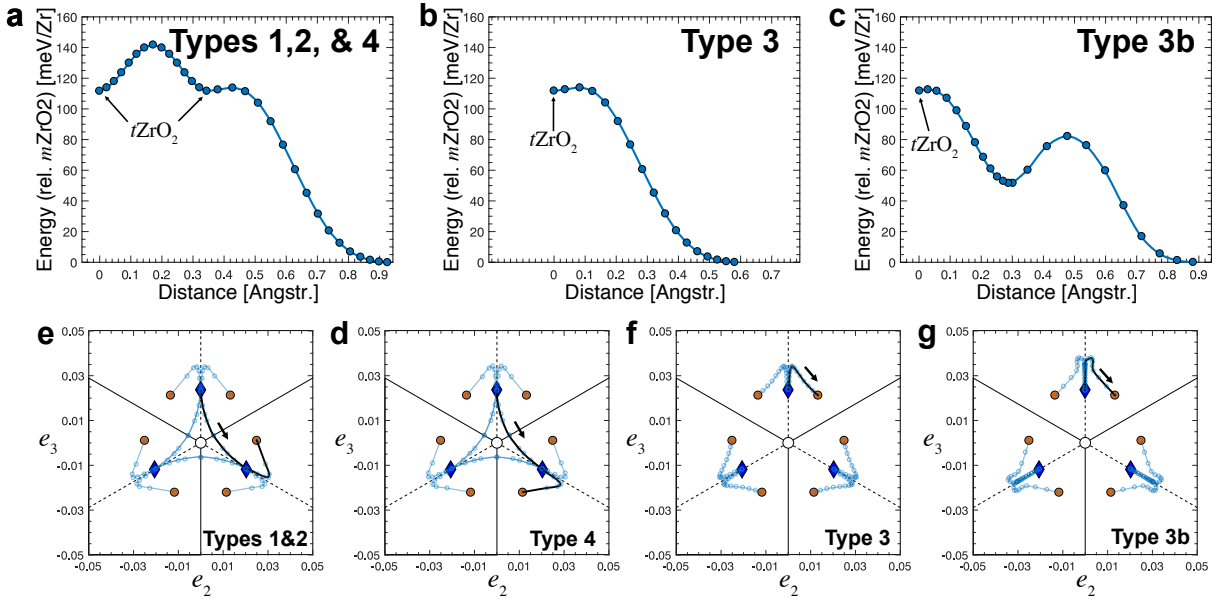


FIG. 8: SSNEB energies along trajectories connecting  $tZrO_2$  and  $mZrO_2$ , corresponding to orientation relationships of (a) types 1 and 2, (b) type 3, and (c) type 3 (along an alternate pathway, denoted 3b). The deviatoric strain is also shown along the pathways corresponding to (d) type 1, (e) type 2, (f) type 3, and (g) type 3 (along the alternate pathy 3b).

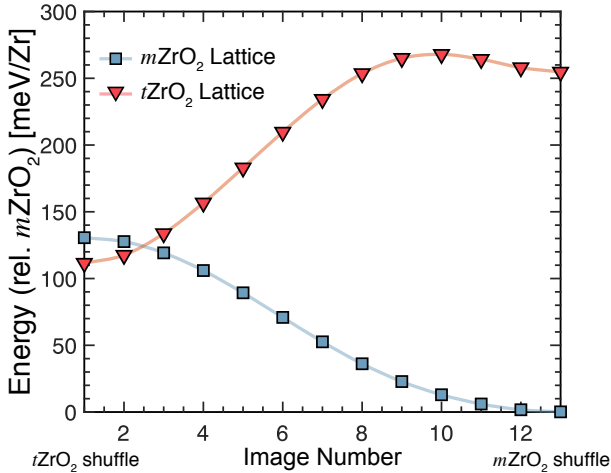


FIG. 9: NEB energy barriers between  $tZrO_2$  and  $mZrO_2$  shuffles calculated at the  $mZrO_2$  lattice vectors (blue squares) and at the  $tZrO_2$  lattice vectors (red triangles).

ilarities to one discovered by Guan *et al.*<sup>46</sup> that is also of the type 3 classification but that passes through an intermediate energy-basin corresponding to an orthorhombic crystal. That intermediate orthorhombic crystal, however, differs from the monoclinic intermediate structure identified here and has an energy of 66.5 meV/Zr above  $mZrO_2$ . This is about 15 meV/Zr higher in energy than the monoclinic crystal depicted in Fig. 7, when the relaxed energies of both structures are calculated using PBE.

The calculations along pathways connecting  $tZrO_2$  and

$mZrO_2$  of Fig. 8(a)-(c) allowed full relaxations of the strain. Both  $tZrO_2$  and  $mZrO_2$ , however, often exist in microstructures that may impose states of large local strain. In order to assess the effect of strain on the stability and kinetic accessibility of  $mZrO_2$  relative to  $tZrO_2$  we calculated energies along NEB trajectories between the  $tZrO_2$  and  $mZrO_2$  internal shuffles at two fixed lattice deformation states. Figure 9 shows the NEB energy along Type 3 trajectories connecting  $tZrO_2$  and  $mZrO_2$  for two fixed deformations. The internal coordinates of the endstate structures were relaxed at the imposed lattice deformations before initializing each trajectory.

The red triangles in Figure 9 were calculated using the  $tZrO_2$  lattice vectors and volume. Although the  $mZrO_2$  internal shuffle increases significantly in energy at the imposed  $tZrO_2$  lattice, becoming unstable relative to the  $tZrO_2$  shuffle, it remains at a metastable minimum that is separated from the  $tZrO_2$  shuffle by a barrier of 12 meV/ZrO<sub>2</sub>. The blue squares in Fig. 9 were calculated using the  $mZrO_2$  lattice vectors and volume. The imposed strain increases the energy of the  $tZrO_2$  shuffle slightly, such that there is no energy barrier with respect to the  $mZrO_2$  shuffle. The  $tZrO_2$  shuffle is thus dynamically unstable under an imposed  $mZrO_2$  strain. Interestingly, the energy penalty due to imposing the  $mZrO_2$  strain on the  $tZrO_2$  internal shuffle ( $\sim 20$  meV/ZrO<sub>2</sub>) is significantly smaller than the increase in energy due to imposing the  $tZrO_2$  strain on the  $mZrO_2$  internal shuffle ( $\sim 250$  meV/ZrO<sub>2</sub>). The increased stiffness of the  $mZrO_2$  shuffle with respect to shear is likely due in part to the distinct topology of the  $mZrO_2$  structure. The shear strain accompanying the  $tZrO_2$ - $mZrO_2$  transformation is essential for accommodating the two distinct oxygen

bonding environments (O3 and O4) in the  $m\text{ZrO}_2$  phase. Straining the monoclinic unit cell of  $m\text{ZrO}_2$  to that of  $t\text{ZrO}_2$  by ‘undoing’ the combined shear ( $e_4/e_5$ ) and deviatoric ( $e_2$ ) strains to obtain a tetragonal lattice requires that the triangles forming O3 layers undergo significant deformation.

#### IV. DISCUSSION AND CONCLUSION

Symmetry-adapted strain and shuffle order parameters are natural variables in Landau free energy descriptions that can feed into modern phase field approaches of structural phase transitions<sup>6,34,47–55</sup>. The order parameters introduced here are capable of distinguishing between different phases and phase variants, including phase variants that have the same orientation but differ by a translation vector of the parent unit cell. This makes it possible to describe not only the martensitic transformation from the parent to the product phase, but also the formation and evolution of twinned microstructures consisting of different orientational and translational variants. Past treatments of the  $t\text{ZrO}_2$ – $m\text{ZrO}_2$  transition already used strain order parameters similar to those introduced here. Fadda et al., for example, introduced a free energy expression in terms of strain order parameters  $e_2$  and  $e_6$  to describe the four *orientational* variants of  $m\text{ZrO}_2$  relative to  $t\text{ZrO}_2$  in a Type 2 orientation relationship<sup>56–58</sup>.

While capable of capturing many attributes of the product phases, thermodynamic descriptions that depend only on strain fail to describe the wide variety of interfaces, including antiphase boundaries and twin boundaries, that are present in coherent microstructures. Furthermore, in the presence of shuffle degrees of freedom there is the possibility of multiple local minima in the free energy surface for a fixed strain state. A clear example of this is the constant-strain NEB calculation shown in Fig. 9 where two local minima exist as a function of internal shuffle degrees of freedom when the unit cell vectors are fixed to those of the tetragonal crystal (i.e. the red triangles). Similar metastable local minima in the (free) energy at fixed strain exist when a cubic lattice is imposed on the  $t\text{ZrO}_2$  shuffle<sup>44</sup>. The existence of multiple local minima as a function of shuffle degrees of freedom for fixed strain is likely to play an important role in the kinetics of microstructure evolution.

The functional dependence of a free energy on strain and shuffle order parameters must be invariant to the symmetry of the parent crystal. Methods for constructing symmetry-invariant free energy expressions are well established<sup>33,59</sup> given the particular symmetry representation of the variables that the free energy depends on. The construction of symmetry representations for the combined strain and shuffle order parameters is described in Appendix A. Free energy models can be constructed phenomenologically using available experimental information or by fitting the coefficients of symmetry-invariant polynomial expressions to first-principles data

obtained via statistical mechanics approaches that are capable of describing the anharmonic vibrational excitations responsible for the structural phase transition<sup>60–62</sup>.

The strain and shuffle order parameters derived specifically for the  $t\text{ZrO}_2$  to  $m\text{ZrO}_2$  phase transition facilitate the analysis and interpretation of the structural pathways connecting different variants of  $m\text{ZrO}_2$  by simplifying the enumeration of symmetrically distinct pairs of monoclinic variants that can coexist in twinned microstructures. Our analysis of the minimum-energy paths between pairs of monoclinic variants has identified low energy forms of  $\text{ZrO}_2$  with local atomic structures that are likely to exist along twin boundaries. These calculations have revealed the importance of O3 layers (layers in which each oxygen is coordinated by three Zr) in low energy forms of  $\text{ZrO}_2$ , including intermediate distorted structures between different variants of  $m\text{ZrO}_2$ . In particular, the monoclinic shear strain of the Zr sublattice that is a feature of  $m\text{ZrO}_2$  is crucial to producing layers having three-fold oxygen coordination.

Surprisingly, the intermediate structure between  $m\text{ZrO}_2$  variants that differ most in their strain state (i.e. the  $(e_5^-, 1)/(e_4^-, 1)$  variant pair) has a very low energy, suggesting that the twin boundary separating such variants may be energetically favorable. The intermediate structure of this variant pair has monoclinic symmetry and an energy that is lower than  $t\text{ZrO}_2$  and many orthorhombic polymorphs of  $\text{ZrO}_2$ . The  $(e_5^-, 1)/(e_4^-, 1)$  variant pair is associated with a (110) twin boundary, which is commonly observed in  $m\text{ZrO}_2$ . The broken symmetries and abrupt changes in bonding environments near twin boundaries and antiphase boundaries can have an influencing role in mass transport and material degradation. Our results suggest that these interfaces likely have distinct and varied structure, which may merit further investigation via methods suited to systematic exploration of the thermodynamic and kinetic properties of interfaces<sup>63–65</sup>.

The strain and shuffle order parameters for  $\text{ZrO}_2$  also help clarify the nature of different pathways connecting  $t\text{ZrO}_2$  and  $m\text{ZrO}_2$ . Strain order parameters are convenient metrics of deformation for exploring different orientation relationships between  $t\text{ZrO}_2$  and  $m\text{ZrO}_2$ . The deviatoric strains,  $e_2$  and  $e_3$ , when referenced relative to the cubic form of  $\text{ZrO}_2$  are especially useful as descriptors to map different pathways that take  $t\text{ZrO}_2$  to  $m\text{ZrO}_2$ . The Type 1 ( $(001)_m \parallel \{100\}_t$  and  $[010]_m \parallel [001]_t$ ) and Type 2 ( $(100)_m \parallel \{100\}_t$  and  $[010]_m \parallel [001]_t$ ) orientation relationships between  $t\text{ZrO}_2$  and  $m\text{ZrO}_2$  require the same deformation of the tetragonal unit cell and therefore follow the same path in  $e_2$  and  $e_3$  space. The strain to achieve these orientation relationships is substantially larger than that needed to achieve the Type 3 ( $(100)_m \parallel \{100\}_t$  and  $[010]_m \parallel \langle 010 \rangle_t$ ) orientation relationship. Plots of minimum energy  $t\text{ZrO}_2$  to  $m\text{ZrO}_2$  pathways in  $(e_2, e_3)$  reveal that the pathways associated with Type 1 and Type 2 orientation relationships are quite long and include two distinct  $t\text{ZrO}_2$  variants, relative to  $c\text{ZrO}_2$ . The Type 3 ori-

entation relationship, in contrast, relates a  $m\text{ZrO}_2$  variant to the  $t\text{ZrO}_2$  variant that is closest in  $(e_2, e_3)$ . Such a ‘nearest neighbor’ crystallographic relationship in strain order parameter space is often the most facile choice for symmetry-breaking phase transitions since other possible relationships typically extend outside the Ericksen-Pitteri neighborhood of the parent crystal<sup>5,66,67</sup>. The Type 3 orientation relationship is commonly observed in experimental measurements of the  $t\text{ZrO}_2$ – $m\text{ZrO}_2$  phase transition<sup>23,45,68</sup> and recent theoretical analysis indicates that the Type 3 orientation relationship may be kinetically favorable compared to other observed orientation relationships<sup>46</sup>.

The approach introduced here to identify symmetry-adapted strain and internal shuffle order parameters for the  $t\text{ZrO}_2$ – $m\text{ZrO}_2$  structural transition can be applied to any group/subgroup structural phase transition. The strain order parameters are expressed as linear combinations of the Hencky strain components in a way that naturally describes symmetry lowering deformations of a parent crystal unit cell having any point group symmetry ???. The combined strain and internal shuffle order parameters naturally emerge from the diagonalization of an orbital covariance matrix, formed by taking the covariance among the atomic displacement vectors of all symmetrically equivalent product phase variants. In the language of group theory, the linear combinations of Eq. 1 project the Cartesian strains onto subspaces that transform according to irreducible representations of the point group of the parent crystal, while the combined strain/shuffle order parameters project the total crystal deformation onto subspaces that transform according to irreducible representations of the space group of the parent crystal. The method is easy to implement, relying on only basic symmetry information, and bears similarities to the widely used statistical technique of principal component analysis<sup>69</sup>. The resulting order parameters yield a minimal set of descriptors that are, by construction, adapted for the space group of the high-symmetry parent reference crystal and optimized for describing the particular transformation under consideration.

### Acknowledgments

This work was supported by the Consortium for Advanced Simulation of Light Water Reactors (<http://www.casl.gov>), an Energy Innovation Hub (<http://www.energy.gov/hubs>) for Modeling and Simulation of Nuclear Reactors under U.S. Department of Energy Contract No. DE-AC05-00OR22725.

Resources of the National Energy Research Scientific Computing Center, a DOE Office of Science User Facility supported by the Office of Science of the U.S. Department of Energy under Contract No. DE-AC02-05CH11231 are gratefully acknowledged, in addition to support from the Center for Scientific Computing at the CNSI and MRL: an NSF MRSEC (DMR-1121053) and

NSF CNS-0960316.

### Appendix A: Symmetry properties of orbital covariance matrix and strain order parameters

An important property of  $\mathbf{C}^{(\bar{D}^*)}$  is that it is invariant to the symmetry of the parent crystal. The application of any space-group operation  $\hat{s}$  to  $\mathbf{Q}^{(\bar{D}^*)}$  simply has the effect of permuting its columns. In matrix form, this implies

$$\hat{s} \left[ \mathbf{Q}^{(\bar{D}^*)} \right] = \mathbf{M}^{(D)}(\hat{s}) \mathbf{Q}^{(\bar{D}^*)} = \mathbf{Q}^{(\bar{D}^*)} \mathbf{W}(\hat{s}), \quad (\text{A1})$$

where  $\mathbf{W}(\hat{s})$  is a  $m \times m$  permutation matrix. Due to the orthogonality of  $\mathbf{M}^{(D)}(\hat{s})$  (i.e.,  $\mathbf{M}^{(D)}(\hat{s})^\top = \mathbf{M}(\hat{s})^{-1}$ ),  $\mathbf{C}^{(\bar{D}^*)}$  transforms as

$$\begin{aligned} \hat{s} \left[ \mathbf{C}^{(\bar{D}^*)} \right] &= \mathbf{W}(\hat{s})^\top \mathbf{Q}^{(\bar{D}^*)\top} \mathbf{Q}^{(\bar{D}^*)} \mathbf{W}(\hat{s}) \quad (\text{A2}) \\ &= \mathbf{Q}^{(\bar{D}^*)\top} \mathbf{M}^{(D)}(\hat{s})^\top \mathbf{M}^{(D)}(\hat{s}) \mathbf{Q}^{(\bar{D}^*)} \\ &= \mathbf{Q}^{(\bar{D}^*)\top} \mathbf{Q}^{(\bar{D}^*)} \end{aligned}$$

which shows that  $\mathbf{C}^{(\bar{D}^*)}$  is invariant to the space group of the parent crystal.

Due to the properties of group invariants<sup>70</sup>, diagonalizing the group-invariant matrix  $\mathbf{C}^{(\bar{D}^*)}$  also simultaneously block-diagonalizes the symmetry representation  $\mathbf{W}(\hat{s})$  of the group to which it is invariant. Thus,

$$\mathbf{M}^{(\eta)}(\hat{s}) = \mathbf{B} \mathbf{W}(\hat{s}) \mathbf{B}^{-1} \quad (\text{A3})$$

is a block diagonal matrix that describes the application of  $\hat{s}$  to transform a vector  $\vec{\eta}$  onto an equivalent vector  $\vec{\eta}' = \mathbf{M}^{(\eta)}(\hat{s}) \vec{\eta}$ . This block-diagonalization implies that the symmetry-adapted order parameters can be partitioned naturally into several symmetry-invariant subspaces (corresponding to the blocks of the symmetry representation). Because the orbit of a particular symmetry-adapted coordinate vector, generated by the parent space group, is restricted to its particular symmetry-invariant subspace, it, in many cases, has higher symmetry than any of the product phase variants that it is used to describe (and from which it was derived). Each symmetry-adapted order parameter subspace is thus associated with a particular type of symmetry-breaking deformation of the parent crystal.

We note that, if the product phase is described in a larger supercell than the parent phase, the shape of the product supercell may break certain symmetries of the parent phase (e.g., a  $2 \times 1 \times 1$  supercell of a cubic supercell can be thought of as having tetragonal symmetry). However, we can always specify the unit cell  $\mathbf{L}^*$  to be the smallest ‘mutually commensurate’ supercell of the parent crystal (i.e., the smallest supercell that can accommodate all equivalent product phase variants). Importantly, a mutually commensurate supercell always preserves all

symmetries of the parent crystal and is the smallest such supercell that is also able to accommodate the displacement field  $\bar{D}^*$ . The mutually-commensurate supercell  $\mathbf{L}^*$  is the unit cell that should be used when applying Eqs. (2) and (3), so that the resulting order parameters are, by construction, invariant to any lattice translation of  $\mathbf{L}^*$ . To account for translations generated by  $\mathbf{L}^{(P)}$  that are not generated by the larger cell  $\mathbf{L}^*$ , we use the effective symmetry group  $S/\mathbf{L}^*$  when applying symmetry, which is a factor group of the space group generated by the left

cosets in  $S$  of the translation group of  $\mathbf{L}^*$ . This group has a finite number of elements (typically a few tens or hundreds), unlike the space group itself, making the application of symmetry a tractable endeavor. The resulting symmetry-invariant free-energy expression is not invariant to arbitrary permutations of atoms, as has been proposed in some formulations of the problem<sup>71,72</sup>, but is instead invariant to all symmetries relevant to reversible deformations of the crystal (i.e., deformations within the Ericksen-Pitteri neighborhood<sup>5,66,67</sup>).

\* Electronic address: johnct@engineering.ucsb.edu

† Electronic address: avdv@engineering.ucsb.edu

<sup>1</sup> A. Khachaturyan, *Theory of structural transformations in solids* (John Wiley and Sons, New York, NY, 1983).

<sup>2</sup> C. M. Wayman, *Metallurgical and Materials Transactions A* **25**, 1787 (1994), ISSN 1543-1940, URL <http://dx.doi.org/10.1007/BF02649029>.

<sup>3</sup> Y. Wang and A. Khachaturyan, *Acta Materialia* **45**, 759 (1997), ISSN 1359-6454, URL <http://www.sciencedirect.com/science/article/pii/S1359645496001802>.

<sup>4</sup> Y. Gao, R. Shi, J.-F. Nie, S. A. Dregia, and Y. Wang, *Acta Materialia* **109**, 353 (2016), ISSN 1359-6454, URL <http://www.sciencedirect.com/science/article/pii/S135964541630026X>.

<sup>5</sup> K. Bhattacharya, S. Conti, G. Zanzotto, and J. Zimmer, *Nature* **428**, 55 (2004), URL <http://dx.doi.org/10.1038/nature02378>.

<sup>6</sup> G. R. Barsch and J. A. Krumhansl, *Phys. Rev. Lett.* **53**, 1069 (1984), URL <http://link.aps.org/doi/10.1103/PhysRevLett.53.1069>.

<sup>7</sup> S. M. Allen and J. W. Cahn, *Acta Metallurgica* **27**, 1085 (1979), ISSN 0001-6160, URL <http://www.sciencedirect.com/science/article/pii/0001616079901962>.

<sup>8</sup> L.-Q. Chen and Y. Wang, *JOM* **48**, 13 (1996), ISSN 1543-1851, URL <http://dx.doi.org/10.1007/BF03223259>.

<sup>9</sup> J. P. Abriata, J. Garcés, and R. Versaci, *Bulletin of Alloy Phase Diagrams* **7**, 116 (1986), ISSN 0197-0216, URL <https://doi.org/10.1007/BF02881546>.

<sup>10</sup> R. Arroyave, L. Kaufman, and T. W. Eagar, *Calphad* **26**, 95 (2002), ISSN 0364-5916, URL <http://www.sciencedirect.com/science/article/pii/S0364591602000275>.

<sup>11</sup> B. P. Burton, A. van de Walle, and H. T. Stokes, *Journal of the Physical Society of Japan* **81**, 014004 (2012), <http://dx.doi.org/10.1143/JPSJ.81.014004>, URL <http://dx.doi.org/10.1143/JPSJ.81.014004>.

<sup>12</sup> B. Puchala and A. Van der Ven, *Phys. Rev. B* **88**, 094108 (2013), URL <https://link.aps.org/doi/10.1103/PhysRevB.88.094108>.

<sup>13</sup> M.-H. Chen, B. Puchala, and A. V. der Ven, *Calphad* **51**, 292 (2015), ISSN 0364-5916, URL <http://www.sciencedirect.com/science/article/pii/S0364591615300353>.

<sup>14</sup> D. Clarke, , and C. Levi, *Annual Review of Materials Research* **33**, 383 (2003), <https://doi.org/10.1146/annurev.matsci.33.011403.113718>, URL <https://doi.org/10.1146/annurev.matsci.33.011403.113718>.

011403.113718.

<sup>15</sup> R. Mévrel, J.-C. Laizet, A. Azzopardi, B. Leclercq, M. Poulain, O. Lavigne, and D. Demange, *Journal of the European Ceramic Society* **24**, 3081 (2004), ISSN 0955-2219, URL <http://www.sciencedirect.com/science/article/pii/S0955221903008616>.

<sup>16</sup> A. Evans, D. Clarke, and C. Levi, *Journal of the European Ceramic Society* **28**, 1405 (2008), ISSN 0955-2219, developments in Ceramic Science and Engineering: the last 50 years. A meeting in celebration of Professor Sir Richard Brook's 70th Birthday, URL <http://www.sciencedirect.com/science/article/pii/S0955221907005948>.

<sup>17</sup> J. M. Dixon, L. D. LaGrange, U. Merten, C. F. Miller, and J. T. Porter, *Journal of The Electrochemical Society* **110**, 276 (1963), <http://jes.ecsdl.org/content/110/4/276.full.pdf+html>, URL <http://jes.ecsdl.org/content/110/4/276.abstract>.

<sup>18</sup> J. W. Fergus, *Journal of Power Sources* **162**, 30 (2006), ISSN 0378-7753, URL <http://www.sciencedirect.com/science/article/pii/S0378775306012110>.

<sup>19</sup> I. Denry and J. R. Kelly, *Dental Materials* **24**, 299 (2008), ISSN 0109-5641, URL <http://www.sciencedirect.com/science/article/pii/S0109564107001133>.

<sup>20</sup> R. C. Garvie, R. H. Hannink, and R. T. Pascoe, *Nature* **258**, 703 (1975), URL <http://dx.doi.org/10.1038/258703a0>.

<sup>21</sup> N. Claussen, *Journal of the American Ceramic Society* **61**, 85 (1978), ISSN 1551-2916, URL <http://dx.doi.org/10.1111/j.1151-2916.1978.tb09237.x>.

<sup>22</sup> A. G. Evans and A. H. Heuer, *Journal of the American Ceramic Society* **63**, 241 (1980), ISSN 1551-2916, URL <http://dx.doi.org/10.1111/j.1151-2916.1980.tb10712.x>.

<sup>23</sup> J. E. Bailey, *Proceedings of the Royal Society of London A: Mathematical, Physical and Engineering Sciences* **279**, 395 (1964), ISSN 0080-4630, <http://rspa.royalsocietypublishing.org/content/279/1378/395.full.pdf>, URL <http://rspa.royalsocietypublishing.org/content/279/1378/395>.

<sup>24</sup> E. Bischoff and M. Rühle, *Journal of the American Ceramic Society* **66**, 123 (1983), ISSN 1551-2916, URL <http://dx.doi.org/10.1111/j.1151-2916.1983.tb09988.x>.

<sup>25</sup> H. Kim, C. O. Chui, K. C. Saraswat, and P. C. McIntyre, *Applied Physics Letters* **83**, 2647 (2003), <http://dx.doi.org/10.1063/1.1613031>, URL <http://dx.doi.org/10.1063/1.1613031>.

<sup>26</sup> H. Kim, P. C. McIntyre, and K. C. Saraswat, *Journal of Materials Research* **19**, 643 (2004).

<sup>27</sup> S. K. Kim and C. S. Hwang, *Electrochem-*

- ical and Solid-State Letters **11**, G9 (2008), <http://esl.ecsdl.org/content/11/3/G9.full.pdf+html>, URL <http://esl.ecsdl.org/content/11/3/G9.abstract>.
- <sup>28</sup> V. Lughi and D. R. Clarke, Surface and Coatings Technology **200**, 1287 (2005), ISSN 0257-8972, {ICMCTF} 2005Proceedings of the 32nd International Conference on Metallurgical Coatings and Thin Films, URL <http://www.sciencedirect.com/science/article/pii/S0257897205007917>.
- <sup>29</sup> V. Lughi and D. R. Clarke, Acta Materialia **55**, 2049 (2007), ISSN 1359-6454, URL <http://www.sciencedirect.com/science/article/pii/S1359645406008159>.
- <sup>30</sup> J. Chevalier, L. Gremillard, A. V. Virkar, and D. R. Clarke, Journal of the American Ceramic Society **92**, 1901 (2009), ISSN 1551-2916, URL <http://dx.doi.org/10.1111/j.1551-2916.2009.03278.x>.
- <sup>31</sup> M. Balog, M. Schieber, M. Michman, and S. Patai, Journal of The Electrochemical Society **126**, 1203 (1979), <http://jes.ecsdl.org/content/126/7/1203.full.pdf+html>, URL <http://jes.ecsdl.org/content/126/7/1203.abstract>.
- <sup>32</sup> C. S. Hwang and H. J. Kim, Journal of Materials Research **8**, 13611367 (1993).
- <sup>33</sup> J. C. Thomas and A. V. der Ven, Journal of the Mechanics and Physics of Solids **107**, 76 (2017), ISSN 0022-5096, URL <http://www.sciencedirect.com/science/article/pii/S0022509616309309>.
- <sup>34</sup> Y. Wang, H. Wang, L.-Q. Chen, and A. G. Khachaturyan, Journal of the American Ceramic Society **76**, 3029 (1993), ISSN 1551-2916, URL <http://dx.doi.org/10.1111/j.1551-2916.1993.tb06605.x>.
- <sup>35</sup> Y. Wang, H.-Y. Wang, L.-Q. Chen, and A. G. Khachaturyan, Journal of the American Ceramic Society **78**, 657 (1995), ISSN 1551-2916, URL <http://dx.doi.org/10.1111/j.1551-2916.1995.tb08228.x>.
- <sup>36</sup> J. P. Perdew, K. Burke, and M. Ernzerhof, Phys. Rev. Lett. **77**, 3865 (1996), URL <http://link.aps.org/doi/10.1103/PhysRevLett.77.3865>.
- <sup>37</sup> G. Kresse and D. Joubert, Phys. Rev. B **59**, 1758 (1999), URL <https://link.aps.org/doi/10.1103/PhysRevB.59.1758>.
- <sup>38</sup> G. Kresse and J. Furthmüller, Phys. Rev. B **54**, 11169 (1996).
- <sup>39</sup> P. E. Blöchl, Phys. Rev. B **50**, 17953 (1994), URL <https://link.aps.org/doi/10.1103/PhysRevB.50.17953>.
- <sup>40</sup> H. J. Monkhorst and J. D. Pack, Phys. Rev. B **13**, 5188 (1976), URL <https://link.aps.org/doi/10.1103/PhysRevB.13.5188>.
- <sup>41</sup> G. Henkelman, B. P. Uberuaga, and H. Jönsson, The Journal of Chemical Physics **113**, 9901 (2000), <http://dx.doi.org/10.1063/1.1329672>, URL <http://dx.doi.org/10.1063/1.1329672>.
- <sup>42</sup> G. Henkelman and H. Jönsson, The Journal of Chemical Physics **113**, 9978 (2000), <http://dx.doi.org/10.1063/1.1323224>, URL <http://dx.doi.org/10.1063/1.1323224>.
- <sup>43</sup> D. Sheppard, P. Xiao, W. Chemelewski, D. D. Johnson, and G. Henkelman, The Journal of Chemical Physics **136**, 074103 (2012), <http://dx.doi.org/10.1063/1.3684549>, URL <http://dx.doi.org/10.1063/1.3684549>.
- <sup>44</sup> M.-H. Chen, J. C. Thomas, A. R. Natarajan, and A. Van der Ven, Phys. Rev. B **94**, 054108 (2016), URL <https://link.aps.org/doi/10.1103/PhysRevB.94.054108>.
- <sup>45</sup> G. Bansal and A. Heuer, Acta Metallurgica **22**, 409 (1974), ISSN 0001-6160, URL <http://www.sciencedirect.com/science/article/pii/0001616074900935>.
- <sup>46</sup> S.-H. Guan, X.-J. Zhang, and Z.-P. Liu, Journal of the American Chemical Society **137**, 8010 (2015), PMID: 26075311, <http://dx.doi.org/10.1021/jacs.5b04528>, URL <http://dx.doi.org/10.1021/jacs.5b04528>.
- <sup>47</sup> D. Fan and L.-Q. Chen, Journal of the American Ceramic Society **78**, 769 (1995), ISSN 1551-2916, URL <http://dx.doi.org/10.1111/j.1551-2916.1995.tb08245.x>.
- <sup>48</sup> D. Fan and L.-Q. Chen, Journal of the American Ceramic Society **78**, 1680 (1995), ISSN 1551-2916, URL <http://dx.doi.org/10.1111/j.1551-2916.1995.tb08870.x>.
- <sup>49</sup> L.-Q. Chen, Annual review of materials research **32**, 113 (2002).
- <sup>50</sup> P. M. Kelly and L. F. Rose, Progress in Materials Science **47**, 463 (2002), ISSN 0079-6425, URL <http://www.sciencedirect.com/science/article/pii/S0079642500000050>.
- <sup>51</sup> A. Finel, Y. L. Bouar, A. Gaubert, and U. Salman, Comptes Rendus Physique **11**, 245 (2010), ISSN 1631-0705, URL <http://www.sciencedirect.com/science/article/pii/S1631070510000794>.
- <sup>52</sup> J. M. Ball and E. C. M. Crooks, Calculus of Variations and Partial Differential Equations **40**, 501 (2011), URL <http://dx.doi.org/10.1007/s00526-010-0349-8>.
- <sup>53</sup> F. Hildebrand and C. Miede, Philosophical Magazine **92**, 4250 (2012), <http://dx.doi.org/10.1080/14786435.2012.705039>, URL <http://dx.doi.org/10.1080/14786435.2012.705039>.
- <sup>54</sup> S. Rudraraju, A. Van der Ven, and K. Garikipati, Npj Computational Materials **2**, 16012 EP (2016), URL <http://dx.doi.org/10.1038/npjcompumats.2016.12>.
- <sup>55</sup> P. Zhao, C. Shen, J. Li, and Y. Wang, Npj Computational Materials **3**, 19 (2017).
- <sup>56</sup> G. Fadda, L. Truskinovsky, and G. Zanzotto, Phys. Rev. B **66**, 174107 (2002), URL <https://link.aps.org/doi/10.1103/PhysRevB.66.174107>.
- <sup>57</sup> G. Fadda, L. Truskinovsky, and G. Zanzotto, Phys. Rev. B **68**, 134106 (2003), URL <https://link.aps.org/doi/10.1103/PhysRevB.68.134106>.
- <sup>58</sup> P. W. Dondl, K. Hormann, and J. Zimmer, Phys. Rev. B **79**, 104114 (2009), URL <https://link.aps.org/doi/10.1103/PhysRevB.79.104114>.
- <sup>59</sup> K. Hormann and J. Zimmer, Journal of the Mechanics and Physics of Solids **55**, 1385 (2007), iD number: ISI:000247888000003, URL <http://opus.bath.ac.uk/6973/>.
- <sup>60</sup> W. Zhong, D. Vanderbilt, and K. M. Rabe, Phys. Rev. B **52**, 6301 (1995), URL <http://link.aps.org/doi/10.1103/PhysRevB.52.6301>.
- <sup>61</sup> J. C. Thomas and A. Van der Ven, Phys. Rev. B **88**, 214111 (2013), URL <http://link.aps.org/doi/10.1103/PhysRevB.88.214111>.
- <sup>62</sup> J. C. Thomas and A. Van der Ven, Phys. Rev. B **90**, 224105 (2014), URL <http://link.aps.org/doi/10.1103/PhysRevB.90.224105>.
- <sup>63</sup> J. C. Thomas, N. A. Modine, J. M. Millunchick, and A. Van der Ven, Phys. Rev. B **82**, 165434 (2010).
- <sup>64</sup> J. C. Thomas, A. Van der Ven, J. M. Millunchick, and N. A. Modine, Phys. Rev. B **87**, 075320 (2013), URL <http://link.aps.org/doi/10.1103/PhysRevB.87.075320>.
- <sup>65</sup> Y.-P. Xie, X.-J. Zhang, and Z.-P. Liu, Journal of the Amer-

- ican Chemical Society **139**, 2545 (2017), pMID: 28166629, <http://dx.doi.org/10.1021/jacs.6b11193>, URL <http://dx.doi.org/10.1021/jacs.6b11193>.
- <sup>66</sup> J. L. Ericksen, *Archive for Rational Mechanics and Analysis* **73**, 99 (1980), ISSN 1432-0673, URL <https://doi.org/10.1007/BF00258233>.
- <sup>67</sup> M. Pitteri, *Journal of Elasticity* **14**, 175 (1984), ISSN 1573-2681, URL <https://doi.org/10.1007/BF00041664>.
- <sup>68</sup> D. K. Smith and W. Newkirk, *Acta Crystallographica* **18**, 983 (1965), URL <https://doi.org/10.1107/S0365110X65002402>.
- <sup>69</sup> I. Jolliffe, *Principal Component Analysis*, Springer Series in Statistics (Springer, 2002), ISBN 9780387954424, URL [https://books.google.com/books?id=\\\_olByCrhjwIC](https://books.google.com/books?id=\_olByCrhjwIC).
- <sup>70</sup> S. Dresselhaus, G. Dresselhaus, and A. Jorio, *Group Theory: Application to the Physics of Condensed Matter*, SpringerLink: Springer e-Books (Springer, 2008), ISBN 9783540328971, URL <http://books.google.com/books?id=sKaH8vrfmnQC>.
- <sup>71</sup> M. Pitteri and G. Zanzotto, *Acta Crystallographica Section A* **54**, 359 (1998), URL <https://doi.org/10.1107/S010876739701667X>.
- <sup>72</sup> M. Pitteri and G. Zanzotto, *Kinematics of multilattices* (Chapman and Hall/CRC, 2002), chap. 11, ISBN 978-0-8493-0327-2, URL <https://doi.org/10.1201/9781420036145.ch11>.